



# Discovery of Eight “Main-sequence Radio Pulse Emitters” Using the GMRT: Clues to the Onset of Coherent Radio Emission in Hot Magnetic Stars

Barnali Das<sup>1</sup> , Poonam Chandra<sup>1</sup> , Matt E. Shultz<sup>2</sup> , Gregg A. Wade<sup>3</sup> , James Sikora<sup>4</sup> , Oleg Kochukhov<sup>5</sup> ,  
Coralie Neiner<sup>6</sup> , Mary E. Oksala<sup>6,7</sup> , and Evelyne Alecian<sup>8</sup>

<sup>1</sup> National Centre for Radio Astrophysics, Tata Institute of Fundamental Research, Pune University Campus, Pune-411007, India; [barnali@ncra.tifr.res.in](mailto:barnali@ncra.tifr.res.in)

<sup>2</sup> Annie Jump Cannon fellow, Department of Physics and Astronomy, University of Delaware, 217 Sharp Lab, Newark, DE 19716, USA

<sup>3</sup> Department of Physics and Space Science, Royal Military College of Canada, PO Box 17000, Station Forces, Kingston, ON K7K 7B4, Canada

<sup>4</sup> Department of Physics & Astronomy, Bishop’s University, Sherbrooke, QC J1M 1Z7, Canada

<sup>5</sup> Department of Physics and Astronomy, Uppsala University, Box 516, SE-751 20 Uppsala, Sweden

<sup>6</sup> LESIA, Paris Observatory, PSL University, CNRS, Sorbonne University, Université de Paris, 5 place Jules Janssen, 92195 Meudon, France

<sup>7</sup> Department of Physics, California Lutheran University, 60 W Olsen Road, Thousand Oaks, CA 91360, USA

<sup>8</sup> University Grenoble Alpes, CNRS, IPAG, F-38000 Grenoble, France

Received 2021 June 18; revised 2021 September 8; accepted 2021 September 8; published 2022 February 1

## Abstract

Main-sequence radio pulse emitters (MRPs) are magnetic early-type stars from which periodic radio pulses, produced via electron cyclotron maser emission (ECME), are observed. Despite the fact that these stars can naturally offer suitable conditions for triggering ECME, only seven such stars have been reported so far within a span of more than two decades. In this paper, we report the discovery of eight more MRPs, thus more than doubling the sample size of such objects. These discoveries are the result of our sub-GHz observation program using the Giant Metrewave Radio Telescope over the years 2015–2021. Adding these stars to the previously known MRPs, we infer that at least 32% of the magnetic hot stars exhibit this phenomenon, thus suggesting that observation of ECME is not a rare phenomenon. The significantly larger sample of MRPs allows us for the first time to perform a statistical analysis comparing their physical properties. We present an empirical relation that can be used to predict whether a magnetic hot star is likely to produce ECME. Our preliminary analysis suggests that the physical parameters that play the primary role in the efficiency of the phenomenon are the maximum surface magnetic field strength and the surface temperature. In addition, we present strong evidence of the influence of the plasma density distribution on ECME pulse profiles. Results of this kind further motivate the search for MRPs, as a robust characterization of the relation between observed ECME properties and stellar physical parameters can only be achieved with a large sample.

*Unified Astronomy Thesaurus concepts:* [Magnetic stars \(995\)](#); [Early-type stars \(430\)](#); [Astrophysical masers \(103\)](#); [Magnetospheric radio emissions \(998\)](#)

## 1. Introduction

Auroral radio emission (ARE) via electron cyclotron maser emission (ECME) has been observed from a wide variety of objects ranging from early-type stars (spectral type B or A; e.g., Trigilio et al. 2000) to cool brown dwarfs and planets (e.g., Hallinan et al. 2006). The observation of this emission from the latter objects is highly useful, as it is one of the best probes with which to estimate magnetic field strengths (since the emission frequency is proportional to the local electron gyrofrequency; e.g., Melrose & Dulk 1982). At the same time, such observations (from cool objects like ultracool dwarfs) are also curious, as the emission requires not only a magnetic field, but also energetic electrons, the source of which is not always apparent. By contrast, in the case of magnetic early-type stars, the situation is somewhat the opposite in the sense that they seem to have all of the ingredients required for the production of ARE. Their magnetic fields often have  $\sim$ kG strengths, have simple topologies (usually well approximated by dipoles; e.g., Kochukhov et al. 2019) and are also highly stable, exhibiting no sign of an intrinsic change over at least thousands of rotational cycles (e.g., Shultz et al. 2018), and only gradually weakening over evolutionary timescales (e.g., Landstreet et al. 2007, 2008; Sikora et al. 2019a; Shultz et al. 2019a). The electrons required for ECM emission are supplied by the stellar wind (those that are energized within the magnetosphere).

Moreover, the global dipole-like magnetic field can produce magnetic-mirror like conditions in which the electrons may undergo a “population inversion,” necessary for maser emission (Trigilio et al. 2000, 2004). Nevertheless, only seven magnetic early-type stars have been observed to produce ECME: CU Vir (Trigilio et al. 2000), HD 133880 (Chandra et al. 2015; Das et al. 2018), HD 142990 (Lenc et al. 2018; Das et al. 2019a), HD 142301 (Leto et al. 2019), HD 35298 (Das et al. 2019b),  $\rho$ Oph A (Leto et al. 2020a), and  $\rho$ Oph C (Leto et al. 2020b). These ECME-producing magnetic early-type stars will be referred as “Main-sequence Radio Pulse emitters” (MRPs, Das & Chandra 2021), as the emission is observed as period radio pulses.

In the past, there has been a suggestion that large deviations of the magnetic field from a dipolar geometry suppresses ECME (Leto et al. 2012). This explanation is however inadequate since there are a number of MRPs, observed to produce ECME, for which the surface magnetic fields have been mapped via “Zeeman–Doppler Imaging” (ZDI) and shown to deviate significantly from that of an axisymmetric dipole (e.g., CU Vir and HD 133880, Kochukhov et al. 2014, 2017). Most recently, Das & Chandra (2021) suggested that a complex magnetic field topology might affect the ECME beaming patterns so that even if a star produces ECME, and exhibits “magnetic null phases” (see Section 2), the radiation may not be visible to an observer over certain frequency

ranges. The role of the magnetic field topology in suppressing ECME is thus vague, and it therefore remains an open question why some stars become MRPs and others apparently do not. One of the biggest hurdles in answering these questions is the very fact that only a small number of such stars are known.

In this paper, we report the discovery of eight new MRPs, more than doubling the size of the MRP population. Our discoveries result from sub-GHz observations carried out with the Giant Metrewave Radio telescope (GMRT) over the years 2015–2021. Combining these with already known MRPs, we, for the first time, present an empirical relation to predict whether a hot magnetic star is likely to produce ECME.

This paper is structured as follows. In the next section (Section 2), we explain what we expect to observe in our radio observations in order to identify an MRP candidate. This is followed by a brief description of the radio data acquisition and analysis (Section 3), and the results for individual stars (Section 4). We discuss the results and summarize our conclusions in Sections 5 and 6, respectively.

## 2. Signature of an “MRP”

In this section, we explain what we expect to see if the star is indeed an MRP. Radio emission from magnetic AB stars is primarily due to the gyrosynchrotron mechanism (e.g., Drake et al. 1987). Such emission (both the total intensity and the percentage of circular polarization) smoothly varies with rotational phase, and the modulation correlates with that of the longitudinal magnetic field averaged over the visible stellar surface  $\langle B_z \rangle$  (e.g., Leone & Umana 1993; Lim et al. 1996; Leto et al. 2020a). It has however been observed that the amplitude of the modulation decreases toward lower radio frequencies (e.g., Leto et al. 2012, 2020a). As will be explained below, when looking for an MRP candidate, the primary signature is a sharp variation of the flux density with rotational phase over a timescale much shorter than that characteristic of the basal gyrosynchrotron emission.

For a star with an oblique axi-symmetric dipolar magnetic field, ECME is produced in ring-shaped regions above the magnetic poles, called “auroral rings” (Trigilio et al. 2011). The direction of emission is tangential to these rings such that the wavevector is perpendicular to the dipole axis (Trigilio et al. 2011). As a result, the emission is expected to be seen when  $\langle B_z \rangle$  is zero (a magnetic null phase), corresponding to the magnetic equator bisecting the visible stellar disk. However, due to propagation effects in the magnetosphere, radiation from opposite magnetic hemispheres, which have opposite circular polarizations, get refracted. Hence, instead of a single pulse composed of radiation from both magnetic hemispheres, visible at the magnetic null phase, we expect to see a pair of oppositely circularly polarized pulses around each magnetic null phase (e.g., Leto et al. 2016). The sequence of arrival of right and left circularly polarized<sup>9</sup> (RCP and LCP, respectively) pulses are opposite near the two magnetic nulls (see Figure 1 of Das et al. 2019a). However, it has now become well known that such idealized behavior is extremely rare. The rotational phases of arrival of the pulses often exhibit significant offsets from the nearest magnetic null phases (Trigilio et al. 2000; Leto et al. 2020a, etc.). Sometimes, pulses of only one circular polarization are observable (e.g., CU Vir, Trigilio et al. 2000). In the past, a very high brightness temperature ( $T_B \gtrsim 10^{12}$  K) and

100% circular polarization were the two criteria for identification of coherent emission (Trigilio et al. 2000; Das et al. 2018). However, as shown by Leto et al. (2016) and Das et al. (2020b), the observed circular polarization depends on propagation effects and, under certain circumstances, can be zero as well. Thus a very high circular polarization is not a necessary condition for the emission mechanism to be identified as ECME. In the case of  $T_B$ , one can only estimate a lower limit since the size of the emission region is not well constrained (Das et al. 2018). Setting the size of the emission site equal to the stellar disk, the expression for the brightness temperature is:

$$T_B \approx 2 \times 10^{13} \times \frac{Sd^2}{\nu^2 R_*^2} \quad (1)$$

where  $S$  is the flux density (in mJy) observed at a frequency  $\nu$  (in MHz) from a star with radius  $R_*$  (in units of solar radii) at a distance of  $d$  (in parsecs). Note that the actual source size is expected to be much smaller than the size of the stellar disk (e.g., Trigilio et al. 2011). Therefore, even if the lower limit turns out to be within the limit of incoherent emission, one cannot use it to rule out ECME. That said, if the lower limit to  $T_B$  is larger than  $10^{12}$  K (the maximum allowed value for incoherent emission), it confirms the emission mechanism to be coherent. In such a case, ECME is almost always favored over plasma emission as the latter cannot explain directed emission. Besides, to give rise to plasma emission at 0.6–0.8 GHz, the required number density is  $\sim 10^9 \text{ cm}^{-3}$ , which is supposed to be present only at the densest part of the stellar magnetosphere (close to the stellar surface, Leto et al. 2006, 2020a).

Based on the above facts, the only condition that we impose to identify an MRP candidate is observation of a significant flux density enhancement over a rotational phase window that encompasses/is close to a magnetic null. The physical reason behind imposing this condition is that ECME is a highly directed phenomenon (e.g., Melrose & Dulk 1982). Since our observations were conducted at sub-GHz frequencies, where we do not expect to see much modulation due to gyrosynchrotron emission (e.g., Leto et al. 2020a), this condition is justified to identify a candidate.

In the ideal case where the gyrosynchrotron modulation follows that of  $\langle B_z \rangle$  (which, in the case of a dipole, varies sinusoidally with rotational phase  $\phi_{\text{rot}}$ ), we can define a necessary condition to attribute an enhancement to ECME. In this case, we approximate the variation of the gyrosynchrotron flux density  $S$  as  $S(\phi_{\text{rot}}) = a \sin^2(2\pi\phi_{\text{rot}}) + b$ , so that  $b = S_{\text{min}}$  and  $a = S_{\text{max}} - S_{\text{min}}$ , where  $S_{\text{min}}$  and  $S_{\text{max}}$  are the minimum and maximum values of  $S(\phi_{\text{rot}})$ , respectively. The maximum gradient of the lightcurve then occurs at  $\phi_{\text{rot}} = 0.125$ , and the maximum value of this gradient is:

$$\left. \frac{dS}{d\phi_{\text{rot}}} \right|_{\text{max}} = 2\pi a. \quad (2)$$

For the lightcurves presented in Section 4, we calculate the quantity  $\Delta S / \Delta\phi_{\text{rot}}$ , where  $\Delta S$  is the change in flux density from the “base” to the peak of an enhancement over the rotational phase range  $\Delta\phi_{\text{rot}}$ . In that case,  $\Delta S \sim a$ , so that the necessary condition to attribute an enhancement to ECME becomes  $1/\Delta\phi_{\text{rot}} > 2\pi$ , or  $\Delta\phi_{\text{rot}} < 0.159$ . We refer to this condition as the “minimum flux density gradient condition.”

<sup>9</sup> We follow the IAU/IEEE convention for circular polarization.

**Table 1**  
Physical Properties of the Eight MRPs Reported Here

HD	Mass ( $M_{\odot}$ )	Radius ( $R_{\odot}$ )	$T_{\text{eff}}$ (kK)	$B_d$ (kG)	Distance (parsec)	$i$ ( $^{\circ}$ )	$\beta$ ( $^{\circ}$ )	Ephemeris	
								HJD <sub>0</sub>	$P_{\text{rot}}$ (d)
12447	$2.6^{+0.2}_{-0.3}$ <sup>a</sup>	$2.7(0.4)$ <sup>a</sup>	$10.0(0.7)$ <sup>a</sup>	$2.4^{+0.7}_{-0.5}$ <sup>b</sup>	$50(2)$ <sup>c</sup>	$38^{+13}_{-9}$ <sup>b</sup>	$86^{+3}_{-4}$ <sup>b</sup>	$2,443,118.328996$ <sup>d</sup>	$1.490975(9)$ <sup>d</sup>
19832	$3.4(0.2)$ <sup>d</sup>	$2.3(0.3)$ <sup>d</sup>	$12.8(0.4)$ <sup>e</sup>	$2.7^{+0.6}_{-0.3}$ <sup>d</sup>	$124(3)$ <sup>c</sup>	$55^{+8}_{-6}$ <sup>d</sup>	$89^{+1}_{-5}$ <sup>d</sup>	$2,442,625.59(9)$ <sup>d</sup>	$0.72776(1)$ <sup>d</sup>
37017	$8.4(0.4)$ <sup>f</sup>	$3.6(0.1)$ <sup>f</sup>	$21(2)$ <sup>d</sup>	$6.2(0.9)$ <sup>f</sup>	$378(11)$ <sup>g</sup>	$38(2)$ <sup>f</sup>	$57(2)$ <sup>f</sup>	$2,443,441.20(9)$ <sup>h</sup>	$0.901186(2)$ <sup>h</sup>
45583	$3.2(0.1)$ <sup>d</sup>	$2.12(0.06)$ <sup>d</sup>	$13.3(0.3)$ <sup>j</sup>	$9.1(0.3)$ <sup>d</sup>	$326(7)$ <sup>c</sup>	$48(2)$ <sup>d</sup>	$70(2)$ <sup>d</sup>	$2,455,521.75(6)$ <sup>d</sup>	$1.17705(1)$ <sup>d</sup>
79158	$4.0(0.2)$ <sup>k</sup>	$3.4(0.7)$ <sup>k</sup>	$13.3(0.3)$ <sup>k</sup>	$3.6(0.4)$ <sup>k</sup>	$175(6)$ <sup>c</sup>	$60(10)$ <sup>l</sup>	$86(2)$ <sup>f</sup>	$2,443,000.45(3)$ <sup>j</sup>	$3.83476(4)$ <sup>l</sup>
145501C	$4.0(0.2)$ <sup>d</sup>	$2.26(0.06)$ <sup>d</sup>	$14.5(0.5)$ <sup>m</sup>	$5.8(0.3)$ <sup>d</sup>	$141(1)$ <sup>c</sup>	$49(3)$ <sup>d</sup>	$89(1)$ <sup>d</sup>	$2,444,774.98(9)$ <sup>d</sup>	$1.02648(1)$ <sup>d</sup>
170000	$3.56^{+0.04}_{-0.49}$ <sup>a</sup>	$3.7(0.1)$ <sup>a</sup>	$11.6(0.1)$ <sup>a</sup>	$1.8^{+0.1}_{-0.2}$ <sup>b</sup>	$93(3)$ <sup>n</sup>	$48^{+5}_{-4}$ <sup>b</sup>	$70^{+4}_{-5}$ <sup>b</sup>	$2,442,632.30626$ <sup>b</sup>	$1.71649(2)$ <sup>p</sup>
176582	$5.6(0.3)$ <sup>f</sup>	$3.21(0.06)$ <sup>f</sup>	$17.6(0.4)$ <sup>d</sup>	$5.4(0.2)$ <sup>f</sup>	$301(4)$ <sup>c</sup>	$84(2)$ <sup>f</sup>	$89.3^{+0.6}_{-1.4}$ <sup>f</sup>	$24,544,96.694(2)$ <sup>h</sup>	$1.581984(3)$ <sup>h</sup>

**Note.**  $T_{\text{eff}}$  is the stellar effective temperature and  $B_d$  is the surface magnetic dipole strength. Terms  $i$  and  $\beta$  correspond to the inclination angle (angle between the stellar rotation axis and the line of sight) and the obliquity (angle between the rotation and dipole axes), respectively. Also given are the reference Heliocentric Julian Day HJD<sub>0</sub>, and the stellar rotation period  $P_{\text{rot}}$ , used to calculate the rotational phases. The values in parentheses represent symmetric error bars.

<sup>a</sup> Sikora et al. (2019b).

<sup>b</sup> Sikora et al. (2019a).

<sup>c</sup> Gaia Collaboration et al. (2018).

<sup>d</sup> Shultz et al. (2020).

<sup>e</sup> Netopil et al. (2008).

<sup>f</sup> Shultz et al. (2019a).

<sup>g</sup> Kounkel et al. (2017).

<sup>h</sup> Shultz et al. (2018).

<sup>j</sup> Semenko et al. (2008).

<sup>k</sup> Wade et al. (2006).

<sup>l</sup> Oksala et al. (2018).

<sup>m</sup> Netopil et al. (2017).

<sup>n</sup> van Leeuwen (2007).

<sup>p</sup> Musielok (1986).

<sup>q</sup> J. Sikora et al. in prep.

<sup>r</sup> This work, see Section 4.5.

### 3. Observations and Data Analysis

The eight stars in our sample, and their properties that are relevant for this study, are listed in Table 1. In the next two subsections, we describe our selection criteria and observation strategy.

#### 3.1. Selection Criteria

All of the stars in our sample have well-characterized magnetorotational properties. In addition, there are a few criteria that were applied to make our sample suitable for our science goal. These are listed below:

1. Based on existing models, ECME is expected to be observable near magnetic null phases (e.g., Trigilio et al. 2011; Leto et al. 2016). Hence, the first criterion that we imposed was that the  $\langle B_z \rangle$  modulation with rotational phase must have at least one magnetic null. Such a condition is realized for  $i + \beta \geq 90^{\circ}$  (the equality condition corresponds to a single magnetic null), where  $i$  is the angle between the line of sight and the rotation axis (inclination angle), and  $\beta$  is the angle between the dipole and rotation axes (obliquity).
2. The next condition arises due to our choice of observing frequency. Our central frequency of observation (0.7 GHz) corresponds to a field strength of 250 G for ECME at the fundamental harmonic (using  $\nu_B \approx 2.8B$ , where  $\nu_B$  is the electron gyrofrequency in MHz and  $B$  is the local magnetic field strength in Gauss). Until now, ECME upper cutoff frequencies have been reported for

only two MRPs: HD 133880 (Das et al. 2020a) and CU Vir (Das & Chandra 2021). In both stars, the upper cutoff frequencies are significantly smaller than the electron gyrofrequency corresponding to the maximum magnetic field strength. For HD 133880, the lowest height corresponding to the upper cutoff frequency is  $\approx 0.6 R_*$  (Das et al. 2020a). In the case of CU Vir, it was not possible to estimate the height due to the complex lightcurves (Das & Chandra 2021). Assuming  $0.6 R_*$  as the minimum height for ECME production, we find that the surface polar strength of the star should be  $> 1$  kG (for emission at the fundamental harmonic). All of the stars in our sample satisfy this condition.

3. For observational convenience, we limited the survey to rapid rotators (rotation periods  $P_{\text{rot}} < 2$  days). The only exception is HD 79158 with  $P_{\text{rot}} \approx 4$  days (Table 1).
4. Since we used the GMRT for our observations, the declinations of the stars must be north of  $-53^{\circ}$ .

#### 3.2. Observation Strategy

The stars were observed at different epochs over the frequency range of 0.6–0.8 GHz with slightly different strategies. In every case, we observed during a range of rotational phases bracketing at least one of the magnetic nulls. The motivation behind this strategy comes from the theoretical prediction that the radio pulses due to ECME will be visible around the magnetic null phases for a star with an axisymmetric dipolar magnetic field (e.g., Leto et al. 2016). Indeed, for the MRPs HD 133880 and HD 35298, the ECME

pulses are observed around their magnetic nulls (Das et al. 2018, 2019b) despite the fact that neither of them has a purely axi-symmetric dipolar magnetic field (Kochukhov et al. 2017; Shultz et al. 2018). However, for the rest of the MRPs, significant offsets (as large as 0.1 rotational phases, Leto et al. 2020a) between the rotational phases of pulse arrival and the nearest magnetic null phase are observed. The possible reasons behind such offsets include incorrect ephemerides, complex surface magnetic fields, and propagation effects in the stellar magnetosphere.

We originally observed the stars only over a narrow rotational phase window ( $\pm 0.03$  rotation cycles). However following reports of offsets larger than this window, we increased the width of the rotational phase window around the magnetic nulls up to  $\pm 0.35$  rotation cycles. In our sample, one star (HD 12447) was observed for nearly one full rotation cycle. Among the remaining stars, two were observed over a rotational phase window of width  $\leq \pm 0.03$  cycles around a magnetic null.

The data were acquired using the GMRT over the years 2015–2021. The earliest data (year 2015) were acquired for the star HD 176582, prior to the upgrade of the observatory. These data span the frequency range 591–624 MHz, divided into 256 channels. The time resolution was 16 s. The rest of the data were acquired over the years 2018–2021 using band 4 (550–950 MHz) of the upgraded GMRT (uGMRT) and have different observation settings. The data acquired during the first half of the year 2018 cover the frequency range of 550–750 MHz, whereas the latter data cover the frequency range of 550–950 MHz. This change in observation setting was a result of the then-ongoing upgrade of the GMRT. Nevertheless, the effective bandwidths (the bandwidth after removing the edges with very low gain) are comparable for the data taken at different epochs. All of the uGMRT data have time resolutions of 8 s. Table 2 details the times of observation, frequency ranges, and the calibrators used in each set of observations.

The data were analyzed using the Common Astronomy Software Applications (CASA, McMullin et al. 2007) following the procedure described by Das et al. (2019a, 2019b).

#### 4. New Stars Displaying ECME Signatures

The lightcurves obtained for the different stars are discussed in the subsequent subsections. For each star, we evaluated the rotational phases using the following equation:

$$\text{HJD} = \text{HJD}_0 + P_{\text{rot}} \cdot E. \quad (3)$$

The reference heliocentric Julian day  $\text{HJD}_0$  and rotation period  $P_{\text{rot}}$  of each star are given in Table 1. In order to identify the magnetic nulls, the rotational modulation of the stellar longitudinal magnetic field  $\langle B_z \rangle$  is fitted with a function of the following form:

$$\langle B_z \rangle = \sum_{n=0}^N B_n \sin(2\pi n \phi_{\text{rot}} + \phi_n). \quad (4)$$

Here,  $\phi_{\text{rot}}$  is the rotational phase and  $N$  is an integer (chosen based on the reduced  $\chi^2$ ).

##### 4.1. HD 12447

HD 12447 is the coolest star in our sample, with an effective temperature of 10 kK (Sikora et al. 2019b). This is also the only

star in our sample that was observed for one full rotation cycle in band 4 of the uGMRT. The rotational and magnetic properties of the star were reported by Borra & Landstreet (1980). The rotation period reported there was 1.4907 days. This was refined further by adding newer measurements of  $\langle B_z \rangle$ , yielding a rotation period of 1.490975(9) days (J. Sikora et al. 2021, in preparation). This rotation period was used to phase both magnetic and radio data (Table 1). We used a sinusoidal function ( $N=1$  in Equation (4)) to model the rotational modulation of  $\langle B_z \rangle$  (top panel of Figure 1). The rotational phases corresponding to the magnetic nulls are  $0.24 \pm 0.02$  and  $0.72 \pm 0.02$ .

As mentioned already, we observed the star for nearly one full rotation cycle. The lightcurves in LCP and RCP are shown in the bottom panel of Figure 1. We find that the star shows significant variability throughout its rotation cycle. We also find the variation to be extremely stable (since we had an overlap in rotational phase ranges covered on different days). This suggests that the underlying phenomenon giving rise to such enhancements is highly stable, both spatially and temporally. The observed variation with rotational phase is, however, quite different from the one that we expect to see due to ECME for a star with an axi-symmetric dipolar magnetic field, in the sense that the enhancements are not particularly confined to regions near the magnetic null phases. However, they are highly unlikely to be of gyrosynchrotron origin for the following reasons:

1. The variation in the radio lightcurve is not smoothly correlated with that of  $\langle B_z \rangle$ .
2. The most notable feature in the lightcurve is the pulse that lies around phase 0.1 (bottom panel of Figure 1). The value of  $\Delta \phi_{\text{rot}}$  over which the LCP pulse reaches its peak from the basal flux density is only 0.02 cycles, significantly smaller than the timescale for variation of the gyrosynchrotron flux density (Section 2). Its peak flux density is nearly an order of magnitude higher than the basal flux density. Gyrosynchrotron emission, however, is not known to vary by such a large amount (an order of magnitude) with stellar rotational phase. The FWHM of this pulse under consideration is  $\approx 0.02$  cycles. The corresponding emission cone can be obtained using the following equation:

$$\cos \alpha = \cos i \cos \beta + \sin i \sin \beta \cos 2\pi(\phi_{\text{rot}} - \phi_0) \quad (5)$$

where  $\alpha$  is the angle between the line of sight and the magnetic dipole axis at a rotational phase  $\phi_{\text{rot}}$ , and  $\phi_0$  corresponds to the rotational phase when the line of sight is closest to the north pole (maximum of  $\langle B_z \rangle$ ). Using  $\phi_0 = 0.477$  (Figure 1), we obtain that the emission is directed over a cone with a half-angle of only  $2^\circ$ . This very high directivity rules out gyrosynchrotron emission completely.

Based on these arguments, we attribute the pulse seen at rotational phase 0.1 to ECME. In that case, the pulse is offset from its “expected” rotational phase of arrival, i.e., the nearest magnetic null phase, by  $\approx 0.1$  cycle (equivalently,  $\approx 70^\circ$  deflection from the magnetic dipole axis). Such offsets are however known to be common among MRPs (Section 3).

It is likely that the remaining weaker enhancements seen in the radio lightcurves at 570–800 MHz are also due to ECME. The FWHM of the enhancements observed around phases 0.6,

**Table 2**  
Observation Details of Our Sample of Stars

HD	Date of Obs.	HJD Range $-2.45 \times 10^6$	Band $\Delta\nu$ (MHz)	Eff. Band $\Delta\nu_{\text{eff}}$ (MHz)	Flux Calibrator	Phase Calibrator
12447	2018-12-28	$8481.10 \pm 0.15$	550-950	570-804	3C48	J0204+152
	2019-11-10	$8798.25 \pm 0.18$	550-950	570-804	3C48	J0204+152
	2019-12-14	$8832.07 \pm 0.04$	550-950	560-814	3C48	J0204+152
	2020-01-02	$8851.23 \pm 0.03$	550-950	570-804	3C48, 3C147	J0204+152
	2020-01-03	$8852.14 \pm 0.16$	550-950	570-804	3C48, 3C147	J0204+152
	2020-01-04	$8853.14 \pm 0.16$	550-950	570-804	3C48, 3C147	J0204+152
	2020-01-05	$8854.14 \pm 0.15$	550-950	570-804	3C48, 3C147	J0204+152
19832	2021-03-27	$9300.86 \pm 0.10$	550-950	570-804	3C48	J0318+164
37017	2018-05-11	$8249.85 \pm 0.03$	550-750	570-667	3C48	J0607-085
	2018-05-12	$8250.93 \pm 0.03$	550-750	560-726	3C147	J0607-085
45583	2020-12-01	$9185.35 \pm 0.12$	550-950	570-804	3C286, 3C48	J0607-085
	2020-12-09	$9193.34 \pm 0.13$	550-950	570-804	3C286, 3C48	J0607-085
79158	2019-11-26	$8813.51 \pm 0.21$	550-950	570-804	3C48, 3C286	J0834+555
	2020-01-31	$8880.31 \pm 0.21$	550-950	570-804	3C48, 3C286	J0834+555
	2021-02-10	$9256.30 \pm 0.22$	550-950	570-804	3C48, 3C286	J0834+555
	2021-02-12	$9258.28 \pm 0.22$	550-950	570-804	3C48, 3C286	J0834+555, J1006+349
	2021-02-27	$9273.25 \pm 0.22$	550-950	570-804	3C48, 3C286	J0834+555, J1006+349
	2021-03-20	$9294.20 \pm 0.23$	550-950	570-804	3C48, 3C286	J0834+555, J1006+349
145501C	2021-03-02	$9275.56 \pm 0.08$	550-950	570-804	3C286	J1626-298
	2021-03-07	$9280.53 \pm 0.15$	550-950	570-804	3C286	J1517-243, J1626-298, J1714-252
	2021-03-17	$9290.49 \pm 0.16$	550-950	570-804	3C286, 3C48	J1517-243, J1626-298
170000	2018-12-17	$8469.84 \pm 0.17$	550-950	570-804	3C48, 3C286	J1634+627
176582	2015-07-27	$7231.24 \pm 0.03$	591-624	594-620	3C286	J1924+334
	2018-06-03	$8272.54 \pm 0.05$	550-750	565-726	3C48	J2015+371

**Note.** HJD stands for Heliocentric Julian Day.

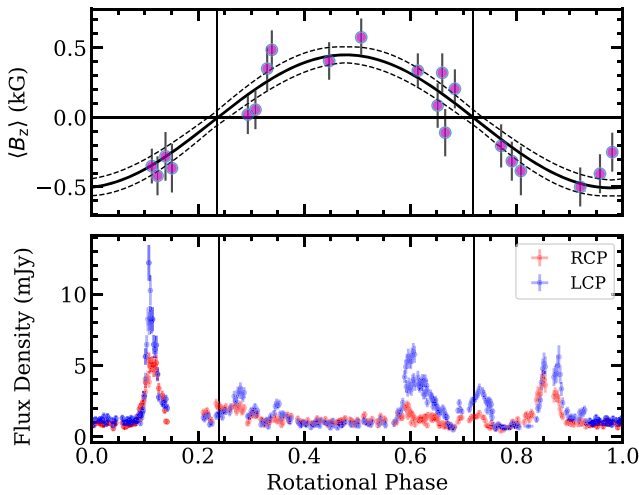


**Figure 1.** Top: the rotational modulation of the  $\langle B_z \rangle$  of the star HD 12447. The data were reported by Borra & Landstreet (1980). The solid curve represents a pure sinusoidal fit and the dashed curves represent the uncertainty associated with this fit. The vertical lines mark the magnetic nulls. Bottom: the lightcurves of the star at 0.6–0.8 GHz for the two circular polarizations.

0.7, and 0.9 correspond to emission over cones with half angles  $6^\circ$ ,  $7^\circ$ , and  $3^\circ$ , respectively, and respectively directed at  $\approx 60^\circ$ ,  $\approx 90^\circ$ , and  $66^\circ$  with respect to the dipole axis. Gyrosynchrotron emission cannot produce such tightly beamed emission. It has been recently reported that the prototypical MRP CU Vir exhibits highly unusual features, attributed to ECME, at sub-GHz frequencies, which are distributed over rotational phases

in a way similar to that we observe for HD 12447 (Das & Chandra 2021). Such behavior could be caused by propagation effects in a magnetosphere with strong plasma density gradients (Das et al. 2020b; Das & Chandra 2021). HD 12447, being a star with large misalignment between its rotation and dipole axes ( $\beta \approx 86^\circ$ ; Sikora et al. 2019b), is likely to satisfy this condition (Townsend & Owocki 2005). Alternatively, the observation of RCP and LCP enhancements over the same rotational phase ranges might be indicative of elliptically polarized emission in the extra-ordinary mode (observed from UV Ceti, Lynch et al. 2017). However our data were not acquired in the full polar mode and hence we are unable to examine the linear polarization of the pulses.

In the future, it will be important to observe the star at higher and lower radio frequencies so as to check how the pulse profiles vary as a function of frequency. For the MRP CU Vir, though it has been found to exhibit peculiar ECME pulses at sub-GHz frequencies, its lightcurves at 1–3 GHz are marked by two narrow, highly circularly polarized ECME pulses. It would be interesting to examine whether HD 12447 shows similar behavior.

#### 4.2. HD 19832

HD 19832 is the most rapidly rotating star in our sample. Its rotational and magnetic properties were recently reported by Shultz et al. (2020). Here, we use the same ephemeris as in Shultz et al. (2020). By fitting a sinusoidal function to the modulation of  $\langle B_z \rangle$  ( $N = 1$  in Equation (4)), we obtain the magnetic null phases to be  $0.178 \pm 0.028$  and  $0.716 \pm 0.028$

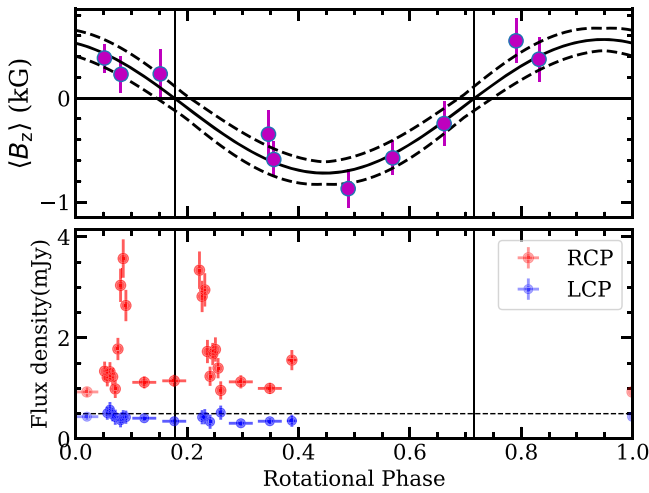


**Figure 2.** Top: the rotational modulation of  $\langle B_z \rangle$  for the star HD 19832 fitted with a sinusoidal function (shown by the solid curve). These data were acquired with the Narval spectropolarimeter at the Bernard Lyot Telescope and reported by Shultz et al. (2020). The dashed curves represent the uncertainties in the fit. The vertical lines mark the magnetic null phases. Bottom: the lightcurves of HD 19832 at 687 MHz.

(top panel of Figure 2). We observed the star in band 4 of the uGMRT near the magnetic null at phase 0.178. The corresponding lightcurves are shown in the bottom panel of Figure 2. As can be seen, there are significant enhancements in RCP flux density, confined to rotational phase windows of width only  $\lesssim 0.06$  cycle (thus satisfying the minimum flux density gradient condition), lying on either side of the magnetic null. The maximum observed circular polarization is  $78 \pm 5\%$ . This, together with the observed sharp variation in flux density, makes it a confirmed MRP. The lower limit to  $T_B$  is  $\sim 10^{11}$  K.

The star shows a highly peculiar variation of flux density in which the “basal” flux density in RCP and LCP are significantly different. Also, there are two separate RCP pulses around the same magnetic null phase. It is worth noting that the star has an obliquity of  $89^\circ$  (Table 1, Shultz et al. 2020). Previously, a double peaked ECME pulse was observed from the magnetic B star HD 142990 (Das et al. 2019a), which interestingly also has an obliquity close to  $90^\circ$  (Shultz et al. 2018). We will discuss this point in Section 5.2.2. The nondetection of an LCP pulse from this star could be due to the fact that the corresponding enhancement appears at a rotational phase not covered by our data. Alternately, the LCP enhancement can have very different cutoff frequencies (as is the case for CU Vir, Das & Chandra 2021). A unique feature observed for this star is the different basal flux densities (over 0.1–0.2 rotational phases) at RCP and LCP. It is possible that the narrow RCP enhancements are superposed on a much broader RCP enhancement. Observation of this star over a full rotation cycle will be highly useful to understand its peculiar behavior.

#### 4.3. HD 37017

HD 37017 is the most distant star in our sample (Table 1). It is in a close binary system with a late B star (Bolton et al. 1998). Shultz et al. (2018) used historical  $\langle B_z \rangle$  measurements (Borra & Landstreet 1979; Bohlender et al. 1987) along with new spectropolarimetric data acquired with the ESPaDOnS spectropolarimeter at the Canada–France–Hawaii Telescope (CFHT) to obtain a rotation period of 0.901186(2) days. They

also found that the rotational modulation of  $\langle B_z \rangle$  for this star can be well modeled by assuming that the star has a centered dipole. This scenario however changed with the subsequent addition of new ESPaDOnS  $\langle B_z \rangle$  measurements (Section Appendix). We found that the combined ESPaDOnS data can be better modeled with the inclusion of a second harmonic to the rotational modulation of the  $\langle B_z \rangle$  function ( $N = 2$  in Equation (4)).<sup>10</sup> The fit along with the  $\langle B_z \rangle$  measurements are shown in the top panel of Figure 3. It can be clearly seen that the magnetic nulls and the maximum of  $\langle B_z \rangle$  are very closely spaced. In fact, based on the actual measurements, it is unclear whether there are indeed two magnetic nulls. At the time of scheduling the radio observations, we did not have access to the newer  $\langle B_z \rangle$  data that reveals the nondipolar nature of the stellar magnetic field. We hence used the null phases predicted by the  $\langle B_z \rangle$  curve of Shultz et al. (2018), which are  $0.41 \pm 0.02$  and  $0.62 \pm 0.03$ . Based on the solid curve in the top panel of Figure 3, the latter rotational phase is rather close to the  $\langle B_z \rangle$  maximum. But as mentioned already, the existence of such a (positive)  $\langle B_z \rangle$  maximum is not well established.

We observed the star near both (supposed) magnetic nulls. The star was detected on both days of our observations. Over the rotational phase window 0.37–0.43 (observed on 2018 May 11), the average flux density (total intensity) is  $0.44 \pm 0.08$  mJy. The RCP flux density is  $0.41 \pm 0.07$  mJy and the LCP flux density is  $0.37 \pm 0.07$  mJy, which are consistent with each other within error bars. We could not examine the time variability of the flux density within the observation duration as the target did not present a sufficient flux density.

Near the other magnetic null, we found the target to be much brighter. The lightcurves (RCP and LCP) corresponding to this magnetic null are shown in the top panel of Figure 3 (red and blue markers near rotational phase 0.6). While the maximum observed circular polarization is only  $37 \pm 11\%$ , this is significantly more polarized than that typically observed for gyrosynchrotron emission at  $\lesssim 1$  GHz (e.g., Leto et al. 2012, 2017, 2018; Das et al. 2018; Das & Chandra 2021). The variability of flux density with rotational phase is significant as well as confined to a narrow rotational phase range (the observation duration was only 0.06 cycles long, clearly satisfying the minimum flux density gradient condition introduced in Section 2), indicating highly directed emission. For the maximum observed flux density  $\sim 1$  mJy, the lower limit to  $T_B$  is  $\sim 10^{11}$  K. If we assume that the basal flux density of the star is  $\approx 0.4$  mJy (the flux density observed near the other magnetic null), the maximum flux density observed here corresponds to an enhancement by a factor of  $\approx 3$ . This makes it an MRP candidate.

In the past, radio observations of this star were reported by Drake et al. (1987), Linsky et al. (1992), Leone & Umama (1993), and Leone et al. (2004). These observations revealed that the star exhibits a positive spectral index ( $S_\nu \propto \nu^\alpha$ ) of  $\alpha = 0.15$  over 1.4–22.5 GHz (Leone et al. 2004). Also, the radio flux density at 5 GHz was found to be modulated with rotation with the maxima coinciding with the  $\langle B_z \rangle$  extrema and the minima coinciding with the null of  $\langle B_z \rangle$ , which is the characteristic of gyrosynchrotron emission (Leone & Umama 1993). Over the full rotation cycle, the flux density was found to vary by a factor of  $\approx 2$  (Linsky et al. 1992; Leone

<sup>10</sup> We did not include the older measurements in the fit to avoid introducing systematics due to the use of different methodologies.

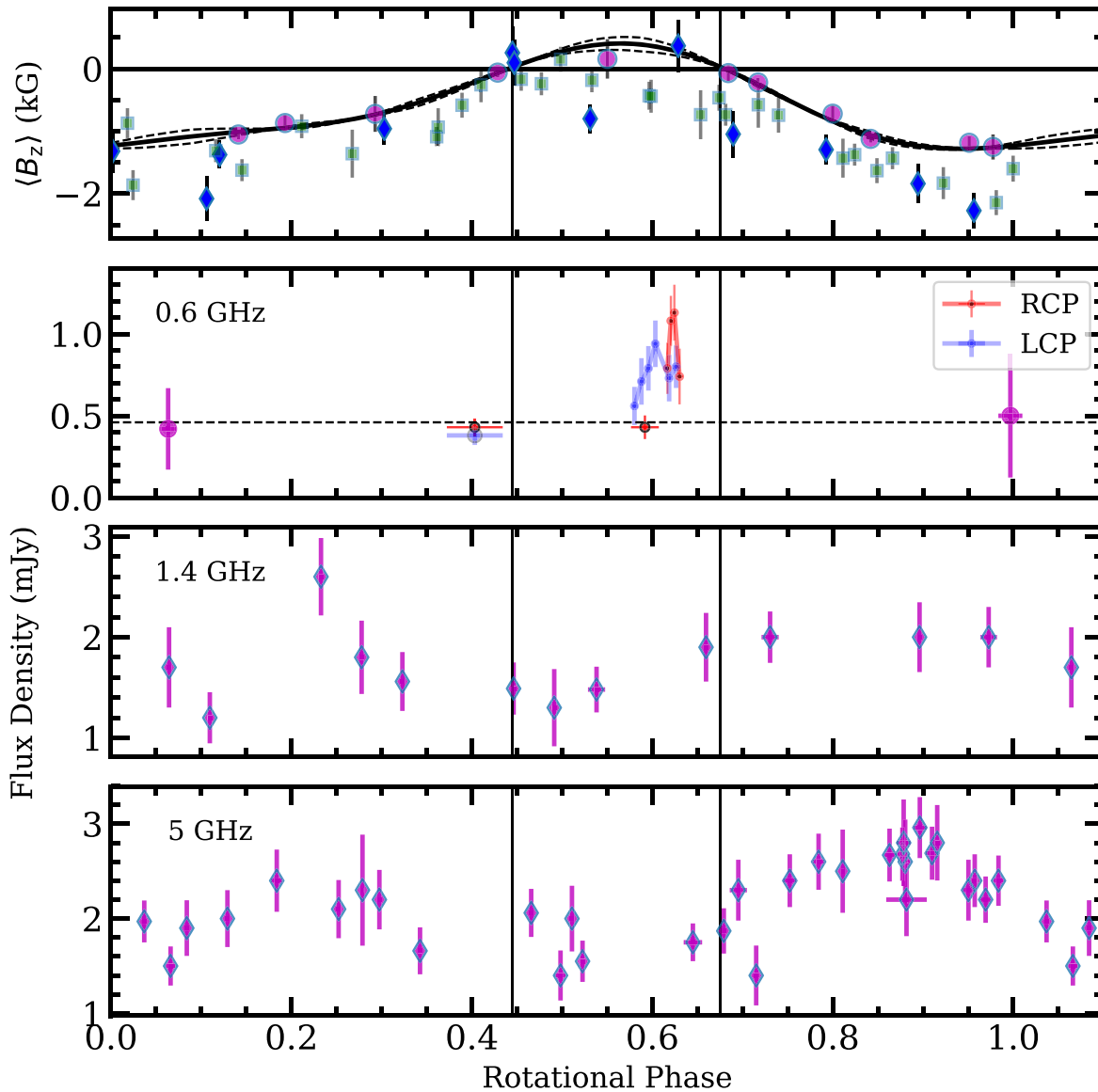


**Figure 3.** The variation of  $\langle B_z \rangle$  and radio flux densities of the star HD 37017 with rotational phase. Top: the  $\langle B_z \rangle$  data for the star. The magenta circles represent data acquired with the ESPaDOnS spectropolarimeter at the Canada–France–Hawaii Telescope (Shultz et al. 2018, see also Section Appendix), the blue diamonds represent data reported by Borra & Landstreet (1979), and the green squares represent data reported by Bohlender et al. (1987). The solid curve represents a function of the form Equation (4) with  $N = 2$  fitted with only the ESPaDOnS measurements. The dashed lines around it shows the uncertainty in the fitting. Bottom three panels: the flux density measurements at different radio frequencies. Except for the red and blue points in the second panel, all other measurements correspond to the total intensity. The vertical lines mark the (supposed) magnetic nulls.

& Umana 1993). Chandra et al. (2015) reported detection of this star at 610 MHz around rotational phase 0.03 (according to the ephemeris used here). Their flux density measurement of  $0.59 \pm 0.32$  mJy is consistent with the flux density that we observed near rotational phase 0.4, and also the basal flux density around the null at phase 0.60. By using a 1.4 GHz measurement at a similar rotational phase, Chandra et al. (2015) obtained a spectral index of  $0.2 \pm 0.1$ , consistent with the value reported by Leone et al. (2004).

In order to understand the significance of the enhancement that we observed in our data, we examined the rotational modulation due to gyrosynchrotron. For that, we reanalyzed all of the archival VLA data at 5 GHz and 1.4 GHz (excluding those that do not have a suitable calibrator). These include data that have not been reported previously to the best of our knowledge, as well as those reported in the past. The resulting

lightcurves are shown in the third and bottom panels of Figure 3. The second panel contains our uGMRT flux densities (red and blue markers representing RCP and LCP, respectively) along with other available measurements (total intensity) at a similar frequency that were also acquired with the GMRT, but before its upgrade (magenta points in the topmost panel of Figure 3, Chandra et al. 2015). In the 5 GHz lightcurve, the rotational modulation is clearly visible. This phenomenon has already been reported by Leone & Umana (1993). But their rotational phase coverage was sparse, and based on those data, Leone & Umana (1993) inferred that the modulation correlates with that of  $\langle B_z \rangle$ , with the maxima of the gyrosynchrotron lightcurve coinciding with the  $\langle B_z \rangle$  minimum, and the minimum coinciding with the null of the  $\langle B_z \rangle$  curve ( $\approx 0.5$  cycles; they assumed that the  $\langle B_z \rangle$  curve only touches zero and never becomes positive, which might in fact be the case as mentioned

already). With the addition of new data, it is now clear that rotational modulation at 5 GHz (and also at 1.4 GHz) is not as simple as had been thought before. It consists of two maxima, each lying between a magnetic null and the  $\langle B_z \rangle$  minimum. Over phases 0.4–0.6, the flux density appears to vary randomly around 1.6 mJy. One of the limitations of all of the past measurements is that they all have significantly larger error bars compared to the new uGMRT measurements. Also, we do not have past measurements around the magnetic null(s). However, based on the observed modulation at 1.4 and 5 GHz, it appears that none of the maxima of the gyrosynchrotron lightcurves occur near the magnetic null(s). In addition, the modulation in the gyrosynchrotron emission occurs over a significantly wider rotational phase window ( $\approx 0.4$  of a rotation cycle), whereas we observed enhancements that are confined to a rotational phase window of width 0.06 cycle only. With decreasing frequency, the amplitude of variability in the gyrosynchrotron emission is expected to decrease (e.g., Leto et al. 2020a; Das & Chandra 2021). Based on these results, we rule out gyrosynchrotron to be the cause of the enhancement seen at 550–800 MHz around phase 0.6. The possibility of free–free emission is also unlikely to cause such a sharp variation with rotational phase (furthermore, the mass-loss rate is too low to give rise to the observed radio emission, Drake et al. 1987). Finally we rule out an origin related to binarity, since neither of the components is expected to have a strong enough wind to give rise to radio emission via wind–wind collision. Hence the only way to produce the enhancements under consideration is via directed emission. Among the magnetic hot stars, ECME is the only known mechanism that satisfies all of these requirements (directed emission, visible near the magnetic null). We therefore attribute the enhancements seen at 550–850 MHz to ECME.

To summarize, the arguments in favor of HD 37017 being a star capable of producing ECME are as follows:

1. The enhancement observed in band 4 occurs over a very narrow range of rotational phases (0.06 cycle only). Gyrosynchrotron is not known to give rise to a systematic variation in flux density over such a small phase window. Besides, the modulation seen for this star at higher radio frequencies confirms that gyrosynchrotron emission varies smoothly and gradually with rotation.
2. The enhancement was observed near/at a magnetic null.
3. Based on our own measurement, the basal flux density in band 4 is  $\approx 0.4$  mJy. Thus we observe an enhancement by a factor of  $\approx 3$ . This is comparable to (but larger than) the magnitude of variation seen due to gyrosynchrotron at higher radio frequencies.

While the star clearly exhibits ECME, the following points require clarification (or need to be examined):

1. Full rotational phase coverage is necessary to clarify the reason behind the absence of any enhancement around the supposed magnetic null at phase 0.4, whether it is offset from that rotational phase, or whether it is indeed absent. The latter will support the idea that  $\langle B_z \rangle$  has only one magnetic null.
2. Though we mentioned that the secondary star of the binary system is unlikely to play a role in the observed emission, it will nevertheless be important to observe the star around its magnetic nulls but at different orbital

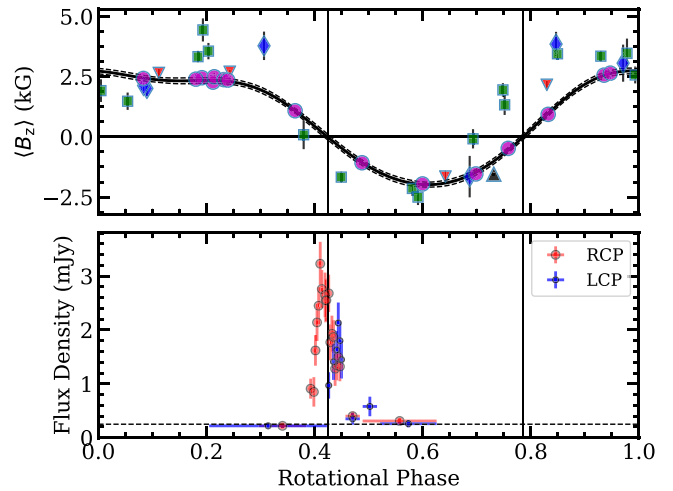


**Figure 4.** Top: the rotational modulation of  $\langle B_z \rangle$  for the star HD 45583. The magenta circles, blue diamonds, the green squares, the black upper triangles, and the red downward triangles correspond to  $\langle B_z \rangle$  data reported by Shultz et al. (2020), Kudryavtsev et al. (2006), Semenko et al. (2008), Bagnulo et al. (2015), and Romanyuk et al. (2017a), respectively. The solid curve corresponds to a function of the form Equation (4) with  $N = 3$ , fitted only to the  $\langle B_z \rangle$  measurements from Shultz et al. (2020); the dashed lines mark the associated uncertainty. The vertical lines mark the magnetic null phases. Bottom: the lightcurves of HD 45583 at 0.6–0.8 GHz. The RCP and LCP enhancements are clearly visible lying around the magnetic null at phase 0.424.

phases. As the data in band 4 were acquired on two consecutive days and the orbital period of the system is  $\approx 19$  days (Bolton et al. 1998), both data sets correspond to similar orbital phases.

In the ideal case of a star with an axi-symmetric dipolar magnetic field, the magnetic null phase lies in between the RCP and LCP pulses (Leto et al. 2016). In the case of HD 37017, the rotational phase where the RCP and LCP pulses intersect is  $\approx 0.62$ , which coincides with one of the magnetic null phases indicated by the  $\langle B_z \rangle$  curve of Shultz et al. (2018). It is however to be kept in mind that for several MRPs, the midpoints between RCP and LCP pulses were found to be offset from the nearest magnetic null phases (e.g., Leto et al. 2019, 2020a; Das & Chandra 2021).

#### 4.4. HD 45583

The magnetic properties of this star have been extensively studied (Kudryavtsev et al. 2006; Semenko et al. 2008; Bagnulo et al. 2015; Romanyuk et al. 2017a; Shultz et al. 2020). To locate the magnetic nulls, we use the measurements reported by Shultz et al. (2020). Rotational modulation of  $\langle B_z \rangle$  exhibits clear signatures of a magnetic field more complex than a simple dipole, or a dipole+quadrupole component (as first noted by Semenko et al. 2008). We fitted a function of the form Equation (4) with  $N = 3$  for  $\langle B_z \rangle$  versus rotational phase (top panel of Figure 4). From the fit, we obtained the magnetic null phases to be  $0.424 \pm 0.007$  and  $0.786 \pm 0.005$ . We observed the star around its null phase 0.424 in band 4 of the uGMRT. The lightcurves at the two circular polarizations are shown in the bottom panel of Figure 4. The star exhibits clear signatures of ECME: there are enhancements in both circular polarizations; both pulses satisfy the minimum flux density gradient condition ( $\Delta\phi_{\text{rot}} < 0.04$ ); the maximum observed circular polarization is  $87 \pm 3\%$ ; and the lower limit to  $T_B$  is

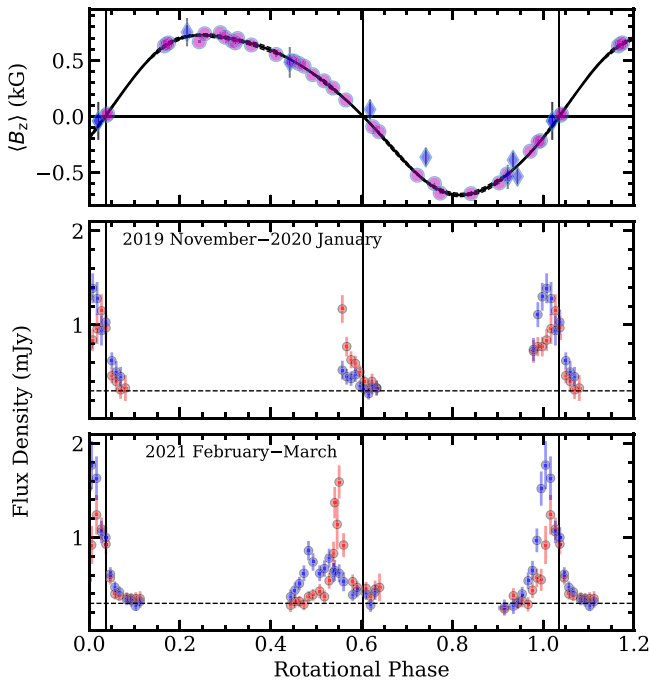


**Figure 5.** Top: the rotational modulation of  $\langle B_z \rangle$  for the star HD 79158. The magenta circles and blue diamonds correspond to  $\langle B_z \rangle$  data reported by Oksala et al. (2018) and Wade et al. (2006), respectively. The solid curve fitted to the  $\langle B_z \rangle$  measurements corresponds to Equation (4) with  $N = 4$ , and fitted only to the data from Oksala et al. (2018). The surrounding dashed lines show the associated uncertainty. The vertical lines mark the magnetic nulls. Middle and bottom: the lightcurves of HD 79158 in band 4 near its magnetic nulls obtained at two epochs. The red and blue markers represent RCP and LCP, respectively.

$3 \times 10^{12}$  K. All of these unambiguously confirm that HD 45583 is another MRP.

#### 4.5. HD 79158

HD 79158 (36 Lyn) is the most slowly rotating star in our sample. Until now, the search for ECME has been limited to more rapidly rotating stars due to observational convenience of achieving rotational phase coverage with a smaller investment in telescope time. HD 79158, with its well-characterized rotation and magnetic properties (Wade et al. 2006; Oksala et al. 2018), is a well-suited starting point to extend the search to longer rotation periods.

The obliquity for HD 79158 in Table 1 was calculated using the inclination angle of Oksala et al. (2018) and the method described in Wade et al. (2006), with an error propagation calculation to determine the uncertainty. However, the ZDI analysis performed by Oksala et al. (2018) revealed that the magnetic field is predominantly dipolar but has a surprisingly large (36%) contributions from a toroidal component. As the method used to calculate the obliquity is derived presuming a simple dipole field structure, the calculation should be considered an estimate rather than a precise value.

In order to locate the nulls of  $\langle B_z \rangle$ , we use  $N=4$  in Equation (4) to fit the  $\langle B_z \rangle$  data (reduced  $\chi^2$  is 3.5). The resulting plot is shown in the top panel of Figure 5. According to this function, the rotational phases corresponding to the magnetic nulls are  $0.036 \pm 0.006$  and  $0.604 \pm 0.008$ . We observed near each of the two magnetic nulls at two epochs using the uGMRT in band 4. The first epoch spans 2019 November to 2020 January, and the second epoch spans 2021

February to March. From these data, we find that the star persistently produces pulses that are visible near its magnetic nulls (second and third panels of Figure 5). The maximum observed circular polarization is  $44\% \pm 7\%$  and the lower limit to  $T_B$  is  $\sim 10^{11}$  K.

Figure 5 shows one interesting characteristic of the radio lightcurves, which is that the radio pulses are significantly broader (e.g., the first enhancement nearly covers 0.2 cycles) than the ECME pulses seen from other MRPs at similar frequencies. However, it has been observed that the pulse width varies from star to star (e.g., Das et al. 2019a, 2019b) and the width increases as we go to lower frequencies (e.g., Das et al. 2020a). In fact, for the star CU Vir, Das & Chandra (2021) observed ECME pulses of similar width over 0.4–0.7 GHz. It is also interesting to find different profiles for pulses of the same polarization but visible at different magnetic nulls (e.g., see the LCP pulses in the bottom panel of Figure 5). Such differences have been observed in the past (e.g., HD 133880; Das et al. 2020a) and could be due to propagation effects in a magnetosphere with an azimuthally asymmetric plasma distribution (Das et al. 2020b, 2020a).

Thus, we suggest that the star HD 79158 produces ECME since:

1. Its lightcurve at our observing frequency shows persistent enhancements in flux density in both RCP and LCP near both magnetic nulls.
2. The enhancements satisfy the minimum flux density gradient condition. The largest  $\Delta\phi_{\text{rot}}$  over which the flux density of an enhancement reaches its peak from its basal value is  $\approx 0.10$  cycles.
3. At our observing frequency (0.6–0.8 GHz), gyrosynchrotron emission is not known to give rise to an order of magnitude enhancement (from  $\approx 0.2$  to 2 mJy) in flux density.

The immediate future work on this star will be to observe it over a wider range of rotational phases and frequencies. The former is especially important as its obliquity is close to  $90^\circ$  (Section 5.2.2). Wideband observation, however, will be able to clarify the point of pulse width at sub-GHz frequencies. In addition, it might be able to help us to understand how the frequency dependence of ECME pulse width varies with stellar parameters.

#### 4.6. HD 145501C

HD 145501C is another magnetic B star of which rotational and magnetic properties were reported by Shultz et al. (2020). The rotational modulation of  $\langle B_z \rangle$  is not well constrained, as there are not sufficient data covering the full rotation cycle (top panel of Figure 6). Here, we fit a function of the form Equation (4) with  $N=2$  to the variation of  $\langle B_z \rangle$  with rotational phase. The magnetic null phases obtained from this fit are  $0.26 \pm 0.04$  and  $0.82 \pm 0.03$ . We however found that the value for the null at which  $\langle B_z \rangle$  changes from negative to positive changes if we fit a different function to the  $\langle B_z \rangle$  data. This is not surprising since there are no data for  $\langle B_z \rangle$  around this magnetic null. The other null phase (phase 0.26 in Figure 6), however, is well constrained. The radio data were acquired around this null (bottom panel of Figure 6). After HD 12447, this star has the highest fractional rotational phase coverage in our sample. As can be seen, the lightcurve in RCP is marked by two very strong enhancements around the magnetic null at phase 0.26.

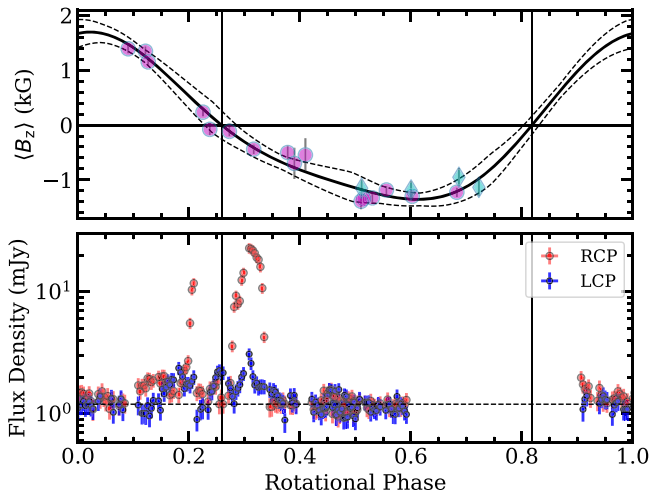


**Figure 6.** Top: the rotational modulation of  $\langle B_z \rangle$  for the star HD 145501C. The measurements corresponding to the magenta points were reported by Shultz et al. (2020) and those corresponding to the cyan points were reported by Borra et al. (1983). The solid curve corresponds to a function of the form given by Equation (4) with  $N = 2$ , and the dashed lines represent error bars associated with the fit. The vertical lines represent the magnetic nulls. As can be seen, the null at phase 0.82 is not constrained by data. Bottom: the radio lightcurves of HD 145501C at 687 MHz covering the magnetic null at phase 0.26 (which is well constrained by data). Note that the y-axis is in log scale. This is done to improve the visibility of the weaker LCP enhancements.

The value of  $\Delta\phi_{\text{rot}}$  over which an enhancement reaches the maximum flux density from the basal level is  $\lesssim 0.04$  cycles, thus satisfying the minimum flux density gradient condition. For the maximum observed flux density,  $T_B > 10^{12}$  K, confirming that it is a result of coherent radio emission. The maximum observed circular polarization is  $76\% \pm 3\%$ . From these observations, we attribute the enhancements to ECME.

In addition to the RCP enhancements, there are also enhancements in LCP that are significantly weaker than their RCP counterparts. Such behavior has been observed in other MRPs also (e.g., HD 133880; Das et al. 2020a).

One of the most interesting observations that we made is the double RCP pulse for this star, similar to that for the stars HD 19832 and HD 142990. All three stars share one common property: they all have obliquities  $\approx 90^\circ$ .

#### 4.7. HD 170000

HD 170000 is the second coolest star in our sample. Its rotation period was recently modified from 1.71649(2) days (Musielok 1986) to 1.71665(9) days (Bernhard et al. 2020). We however find this new period to be unable to consistently phase  $\langle B_z \rangle$  data acquired at widely separated epochs (Landstreet & Borra 1977; Sikora et al. 2019a). We hence chose to use the older rotation period for phasing both magnetic and radio data. The top panel of Figure 7 shows the rotational modulation of  $\langle B_z \rangle$  data along with the fit (of the form Equation (4) with  $N = 2$ ) The magnetic null phases according to this fit are  $0.298 \pm 0.005$  and  $0.659 \pm 0.008$ .

We observed this star around its magnetic null at phase 0.66. The lightcurves that we obtained are shown in the bottom panel of Figure 7. We find a significant enhancement in LCP flux density with  $\Delta\phi_{\text{rot}} \approx 0.10$  cycles (thus satisfying the minimum flux density gradient condition, Section 2), right at the magnetic null phase. In addition, there is also an indication of an enhancement in RCP ahead of the start of the rotational

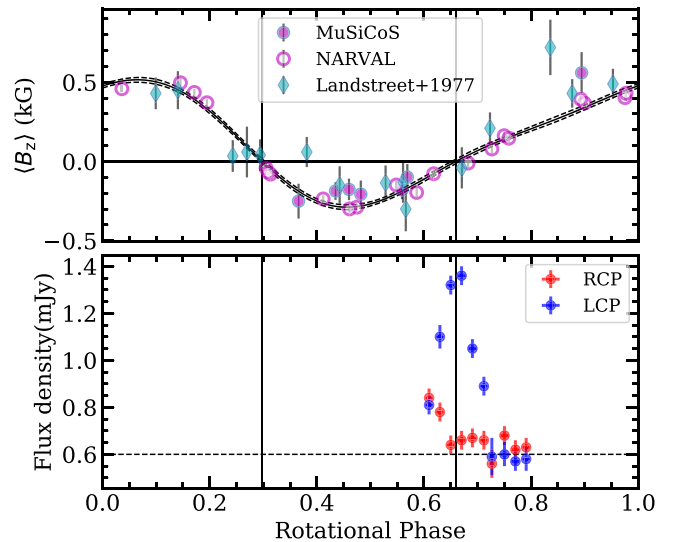


**Figure 7.** Top: the  $\langle B_z \rangle$  variation with rotational phase for the star HD 170000. We fit the data with a function of the form Equation (4) with  $N = 2$  (solid curve). The dashed lines represent the uncertainty in the fit. The magenta points represent data reported by Sikora et al. (2019a) and the cyan points represent data reported by Landstreet & Borra (1977). Bottom: the lightcurves of HD 170000 at 687 MHz. The vertical lines represent magnetic null phases.

phase window covered by our observation. The maximum observed circular polarization is  $35\% \pm 3\%$  and the lower limit to  $T_B$  is  $\sim 10^{10}$  K. Based on the observation of a flux density enhancement confined to a rotational phase window of width  $\sim 0.1$  cycles around a magnetic null phase, we suggest that the star is an MRP. In addition, circular polarization as high as 35% at sub-GHz frequencies and at a magnetic null phase goes against the idea of gyrosynchrotron.

In the future, observation over a broader rotational phase window near both magnetic nulls will be highly useful to understand the properties of coherent radio emission observed from this star.

#### 4.8. HD 176582

The magnetic field in HD 176582 and its co-rotating magnetosphere was first discovered by Bohlender & Monin (2011). For this star also, Shultz et al. (2018) proposed the presence of higher-order moments in the magnetic field. The  $\langle B_z \rangle$  modulation with rotational phase, fitted with a function of the form given by Equation (4) with  $N = 3$  is shown in the top panel of Figure 8. According to the fitted  $\langle B_z \rangle$  function, the rotational phases corresponding to the magnetic nulls are  $0.491 \pm 0.003$  and  $0.990 \pm 0.002$ . We observed the star around phase 0.5 using the legacy GMRT at 0.6 GHz in the year 2015. In addition, we observed the star around phase 0.8 using the band 4 (550–800 MHz) of the uGMRT in the year 2018. The latter rotational phase is close the rotational phase corresponding to the  $\langle B_z \rangle$  maximum.

In the bottom panel of Figure 8, we show the radio flux density measurements. The GMRT data clearly show a very strong enhancement near a magnetic null. The fact that the flux density observed at the null is higher by a factor of  $\gtrsim 4$  than that observed around a  $\langle B_z \rangle$  maximum, and that the enhancement shows a sharp change in flux density over a narrow rotational phase window ( $\Delta\phi_{\text{rot}} \approx 0.03$  cycles, satisfying the minimum flux density gradient condition), strongly suggest that the star is also an MRP. We next calculate the lower limit to  $T_B$ , setting

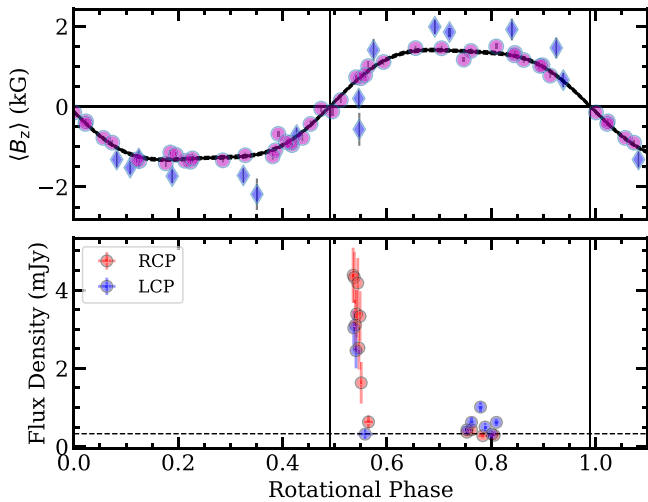


**Figure 8.** Top: the rotational modulation of  $\langle B_z \rangle$  for the star HD 176582. The magenta circles and blue diamonds correspond to data reported by Shultz et al. (2018) and Bohlender & Monin (2011), respectively. The vertical lines correspond to magnetic nulls. The solid curve corresponds to the function given by Equation (4) with  $N = 3$ , fitted only with the data from Shultz et al. (2018). Bottom: the lightcurves of HD 176582 over 0.6–0.7 GHz. The data around the phase 0.5 were acquired using the legacy GMRT, whereas the other data were acquired using the uGMRT.

the source size to be comparable to the stellar disk. For the maximum observed flux density ( $\approx 4$  mJy), we find  $T_B > 2 \times 10^{12}$  K, implying that the emission is of coherent origin. This, together with the fact that the enhancement was observed near a magnetic null, confirms HD 176582 to be an MRP.

The rotational phases corresponding to the maximum observed flux density is offset by  $\approx 0.05$  cycles from the nearest magnetic null phase. However past observations have shown that such offsets are rather common among the MRPs. Offsets as large as 0.1 cycles have been reported in the rotational phases of arrival of ECME (Leto et al. 2020a). Note that this star also has an obliquity close to  $90^\circ$  (Table 1). Unfortunately, we do not have sufficient rotational phase coverage to infer anything about the pulse profile. In the future, this star is worth observing over a broader rotational phase window near both magnetic nulls.

## 5. Discussion

With the addition of eight more magnetic hot stars to the list of known MRPs, the number of such stars has more than doubled from 7 to 15. Among the newly added stars, HD 12447 becomes the nearest known MRP (50 pc, Table 1), surpassing CU Vir, which is at a distance of 72 pc (Gaia Collaboration et al. 2018). The same star (HD 12447) is also the coolest MRP ( $T_{\text{eff}} \approx 10$  kK, Table 1) known so far. This work also introduces the most slowly rotating MRP HD 79158 (Table 1). Our results therefore significantly expand the stellar parameter space of magnetic stars which can produce ECME.

In the following subsections, we discuss some of the key conclusions that we are able to draw from this work.

### 5.1. The Incidence of MRPs among Magnetic Hot Stars

The large number of ECME detections reported here, more than doubling the number of known MRPs, suggests that the phenomenon of ARE may be more common among magnetic

early-type stars than previously supposed. In order to quantify this, we searched the literature for the known magnetic hot stars. The major studies consulted were the following: the studies of Ap, He-weak, and He-strong stars by Borra & Landstreet (1979, 1980), Borra et al. (1983), and Bohlender et al. (1987, 1993); the slowly rotating Ap star study of Landstreet & Mathys (2000); the study of Ap stars by Aurière et al. (2007); the sample of Ap stars in open clusters presented by Landstreet et al. (2007, 2008); the Herbig Ae/Be stars studied by Alecian et al. (2013); the Of?p stars examined by Petit et al. (2013) and Munoz et al. (2020); the early B-type stars presented by Shultz et al. (2018, 2019b, 2020); the volume-limited sample of Ap stars conducted by Sikora et al. (2019b, 2019a); the samples of stars with magnetically split lines examined by Mathys (2017) and Chojnowski et al. (2019); and the results of the ongoing survey at the Special Astrophysical Observatory of both field stars (Kudryavtsev et al. 2006; Romanyuk et al. 2014, 2015, 2016a, 2017a, 2018; Romanyuk 2019; Romanyuk et al. 2020) and stars in the Orion nebula (Romanyuk et al. 2016b, 2017b, 2019, 2021). The compilation of longitudinal magnetic field curves provided by Bychkov et al. (2021) was also consulted, in order to include magnetic stars reported in single-star papers.

The full catalog consists of 765 stars with at least one magnetic measurement. Comparison to this population yields an incidence fraction of just under 2%. However, ARE can only be detected in stars with magnetic nulls; for the majority of stars in the sample only individual magnetic measurements are available, and it is therefore unknown whether these stars exhibit magnetic nulls. Furthermore, with the exception of HD 79158, our survey was limited to stars with  $P_{\text{rot}} < 2$  days, whereas many magnetic stars have periods much longer than this. Finally, ARE has been detected only in stars with  $T_{\text{eff}} \geq 10$  kK, likely because cooler stars do not possess strong enough winds to populate their magnetospheres with a sufficient electron density to generate radio emission (and, indeed, incoherent gyrosynchrotron has not been detected from such stars; e.g., Drake et al. 1987; Linsky et al. 1992). It is therefore necessary to limit the comparison sample to stars occupying the same parameter space as the stars of the survey.

When effective temperatures were not available in the above studies, we consulted the compilations presented by Kochukhov & Bagnulo (2006), Netopil et al. (2017), and Moiseeva et al. (2019). When not available in those studies, we cross-referenced with the Strömgren photometric catalog published by Paunzen (2015), utilizing the IDL program UVBYBETA (which implements the calibration determined by Napiwotzki et al. 1993), with the calibration set by the Simbad spectral type. If Strömgren photometry was not available, we utilized the Johnson photometric colors obtained from Simbad together with the empirical color tables given by Worthey & Lee (2011), with reddening values found using the *Stilism* three-dimensional tomographic dust map (Lallement et al. 2014; Capitanio et al. 2017; Lallement et al. 2018) and distances from Gaia early Data Release 3 parallaxes (Gaia Collaboration et al. 2021).

In the end the catalog contains 245 stars for which the  $T_{\text{eff}}$ , rotation period, and ORM parameters are all available, of which MRPs comprise about  $6 \pm 2\%$ . However, there are only 43 stars with  $9.3 < T_{\text{eff}} < 23$  kK (the  $T_{\text{eff}}$  range in our sample when uncertainties are accounted for),  $P_{\text{rot}} < 2$  days, and the presence of magnetic nulls in their  $\langle B_z \rangle$  curves, of which MRPs

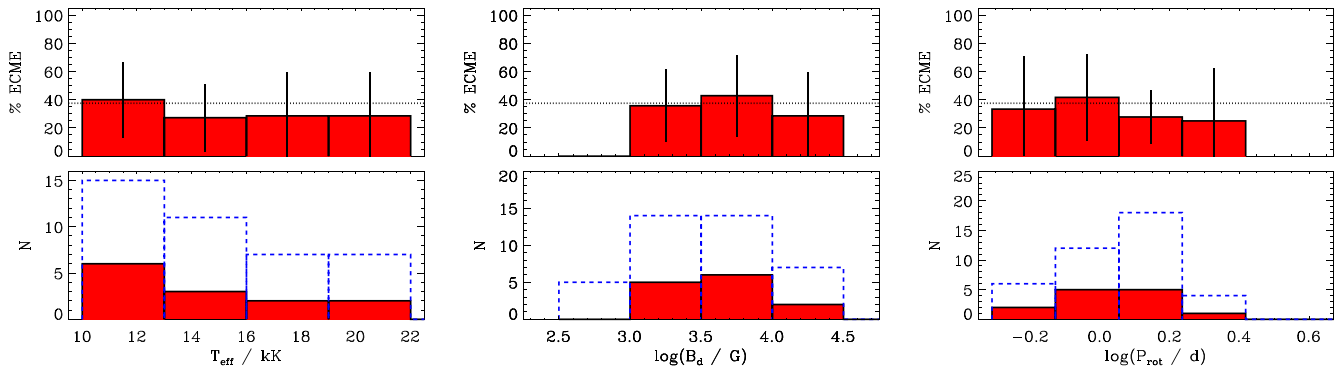


**Figure 9.** Histograms of  $T_{\text{eff}}$  (left),  $B_d$  (middle), and  $P_{\text{rot}}$  (right) for the percentage incidence of MRPs (top). The absolute numbers are shown in the bottom panels with dashed blue bars representing the number of all of the comparison stars and the solid red bars representing the number of MRPs.

comprise  $32 \pm 14\%$ . We note that this already high fraction is a conservative lower boundary: many of the stars have not been observed for ECME, since, e.g., their magnetic fields or rotation periods were only reported within the last couple of years; furthermore, of those that have, but in which ECME has not yet been detected, it cannot yet be ruled out that the pulses were missed due to either errors in the ephemerides, or phase offsets from the expected occurrence at the magnetic null.

Figure 9 shows histograms of  $T_{\text{eff}}$ ,  $B_d$ , and  $P_{\text{rot}}$  for the comparison population and MRPs. The  $T_{\text{eff}}$  distribution of MRPs closely follows that of the comparison population, with an incidence fraction consistent with no variation with  $T_{\text{eff}}$ . There are no MRPs with  $B_d < 1$  kG, which is likely a consequence of the choice of observing frequency (Section 3.1). Above this the incidence fraction is consistent with a flat distribution. To explore the possibility of ECME in stars with  $B_d < 1$  kG, one will have to go to frequencies smaller than 0.7 GHz. There is some suggestion that the incidence falls off with slower rotation, however it is consistent with a flat distribution within uncertainties. We, however, would like to emphasize that the fact that all of the known MRPs are relatively rapid rotators is a result of observational convenience (see point 3 of Section 3.1). Thus within the parameter space spanned by the MRPs, there seems to be no preference for any subgroup of stellar parameters in terms of incidence fraction. This scenario might change with the discovery of more MRPs in the future.

## 5.2. Comparing Physical Properties of the MRPs Discovered

One of the prime motivations for continuing to search for MRPs is to have a sample large enough so as to be able to compare their physical properties and find answers to questions like what type of magnetic hot stars produce ECME. With our addition of eight MRPs, the number of MRPs known have gone up to 15. Though it cannot be called a “large” sample, we still attempt, for the first time, an investigation of the emission properties of the population and how they correlate to previously determined stellar, magnetic, and rotational parameters. Below we present the results from this exercise.

### 5.2.1. Onset of ECME

As a first step, we compare the luminosity corresponding to the peak flux density of the ECME pulses for all of the known MRPs. Note that the peak flux density corresponds to one of the two circular polarizations and not the total intensity. We use the quantity  $S_{\text{peak}} \times d^2$  as a proxy for the peak luminosity,

where  $S_{\text{peak}}$  is the “excess” peak flux density (with respect to the basal flux density due to gyrosynchrotron) and  $d$  is the distance to the star. In the case of HD 147932 (also known as  $\rho$  Oph C), no estimate for the basal flux density could be obtained, which is due to the fact that the obliquity is likely zero implying that ECME is observable at all rotational phases (Leto et al. 2020b). Therefore, HD 147932 is not included in our analysis. Barring the stars HD 142301 (3 Sco) and HD 147933 ( $\rho$  Oph A), the peak flux densities correspond to the ECME pulses observed over 0.6–0.8 GHz (i.e., the band 4 of the uGMRT and the 610 MHz of the legacy GMRT). Das & Chandra (2021) recently reported sub-GHz observations for the MRP CU Vir. On one of the days of observation, they witnessed a “giant pulse” in band 4 of the uGMRT, which was an order of magnitude brighter than the typical pulses observed from this star. This phenomenon is very likely a transient event and, hence, we have not used this pulse in the analysis presented in this paper. However, the qualitative picture does not change even if we include this giant pulse. For HD 142301, we use its peak flux density at 1.5 GHz reported by Leto et al. (2019). For HD 147933, we use the peak flux densities at 2.1 GHz reported by Leto et al. (2020a).

We examine the variation of the quantity  $S_{\text{peak}} d^2$  with stellar mass  $M_*$ , radius  $R_*$ ,  $T_{\text{eff}}$ , rotation period  $P_{\text{rot}}$ , and the maximum magnitude of the surface magnetic field strength  $B_0^{\text{max}}$ <sup>11</sup> (Figure 10). Note that  $M_*$  is correlated with  $R_*$  and  $T_{\text{eff}}$ . Nevertheless, we find the tightest correlation of  $S_{\text{peak}} d^2$  with  $T_{\text{eff}}$  and the weakest (or no) correlation with  $R_*$  among the three quantities (Figure 10). Similarly, we find that the peak luminosity and  $B_0^{\text{max}}$  are correlated. With  $P_{\text{rot}}$ , we do not find any correlation with the peak ECME luminosity. This however cannot be trusted since MRPs discovered so far essentially span only a very narrow range of stellar rotation periods.

From Figure 10, we find that the relation between the quantity  $\log(S_{\text{peak}} d^2)$  and  $T_{\text{eff}}$  is nearly a parabola with a vertex ( $T_0$ ) around 15–18 kK. To locate  $T_0$  more precisely, we calculated the Spearman’s rank correlation coefficient<sup>12</sup>  $\rho$  (Dodge 2008) between the quantities  $S_{\text{peak}} d^2$  and  $(T_{\text{eff}} - T_0)^2$ , varying  $T_0$  between 15 and 18 kK (with a step size of 0.5 kK).

<sup>11</sup> This is not necessarily the same as the dipole strength; e.g., for the star CU Vir, the maximum magnetic field strength is 1–2 kG at the north pole and 4 kG at the south pole (Kochukhov et al. 2014). In such a case, we take  $B_0^{\text{max}} = 4$  kG.

<sup>12</sup> Spearman’s rank correlation can assess monotonicity of a relation, and is thus more general than the Pearson correlation coefficient, which can assess only a linear relation. For a perfect correlation or anti-correlation, the correlation coefficient (denoted by  $\rho$ ) is  $\pm 1$  with a  $p$ -value of zero.

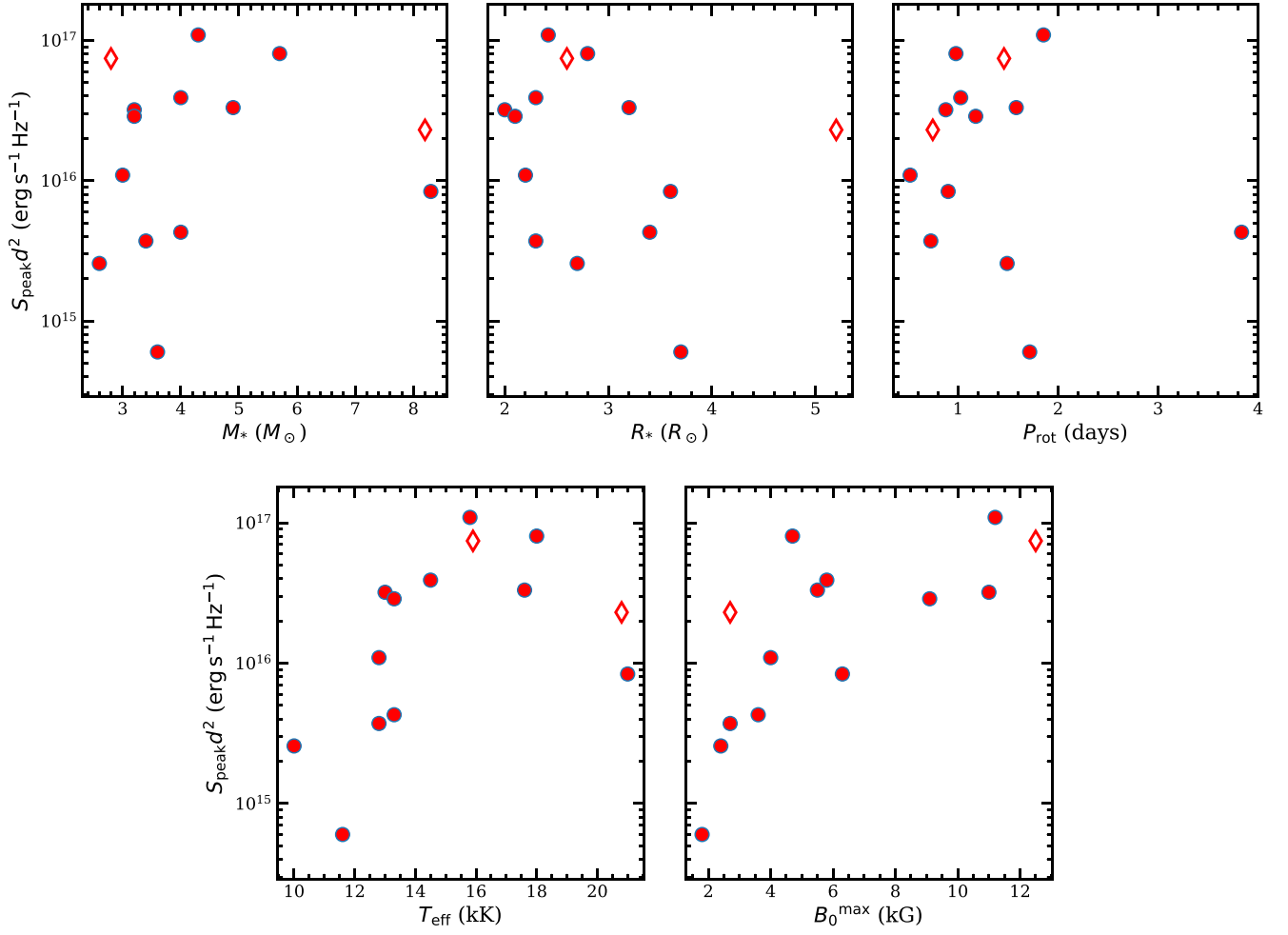


**Figure 10.** Variation of the quantity  $S_{\text{peak}} d^2$  (proxy for the peak ECME luminosity; Section 5.2.1) with stellar mass  $M_*$ , radius  $R_*$ , rotation period  $P_{\text{rot}}$ , effective temperature  $T_{\text{eff}}$ , and the maximum magnitude of the surface magnetic field strength  $B_0^{\text{max}}$ . The filled circles represent data at frequencies 0.6–0.8 GHz (GMRT data), whereas the two open diamonds, which correspond to the stars HD 142301 (Leto et al. 2019) and HD 147933 (Leto et al. 2020a), represent data taken at 1.5 and 2.1 GHz, respectively.  $S_{\text{peak}} d^2$  corresponds to the maximum flux density observed from a star at any of the two circular polarizations.

This procedure yields  $T_0 = 16.5$  kK. The corresponding value of  $\rho$  is  $-0.88$  with a  $p$ -value of 0.0001. A similar exercise with stellar mass yields  $\rho = -0.60$  with a  $p$ -value of 0.04. Thus, our preliminary analysis with the sample of 12 MRPs (excluding HD 142301, HD 147932 and HD 147933) suggests that the peak ECME luminosity is a maximum among magnetic hot stars with  $T_{\text{eff}} \approx 16.5$  kK. In the case of the correlation with magnetic field strength, the Spearman’s rank correlation coefficient is  $+0.76$  with a  $p$ -value of 0.004.

Based on the above results, we construct the quantity  $X = B_0^{\text{max}} / (T_{\text{eff}} - 16.5)^2$  and plot the proxy for the peak ECME luminosity against this quantity. Figure 11 shows the result. As expected, we find a much tighter correlation between the peak luminosity and  $X$  with  $[\rho, p] = [0.94, 4 \times 10^{-6}]$  without including  $\rho$  Oph A and HD 142301. Including the latter two stars slightly degrades the correlation giving  $[\rho, p] = [0.90, 10^{-5}]$ . By fitting a power law to this relation (again excluding HD 142301 and HD 147933), we obtain that the peak ECME luminosity  $\propto X^{0.8 \pm 0.1}$ . With more discoveries of MRPs, it will be possible to check whether such a relation indeed holds true.

We now consider possible explanations for the observed correlation. At first sight, the correlation between the peak ECME luminosity and the maximum surface magnetic field might look obvious given that the magnetic field is the primary

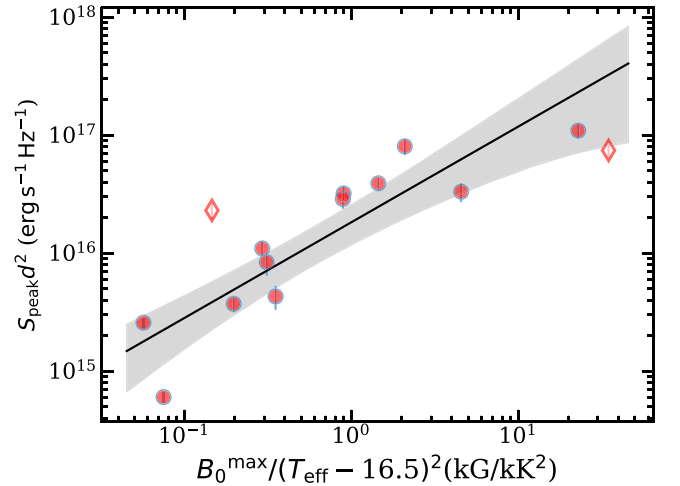


**Figure 11.** The derived relation between peak ECME luminosity (represented by  $S_{\text{peak}} \times d^2$ ), maximum magnitude of the surface magnetic field  $B_0^{\text{max}}$ , and the surface temperature  $T_{\text{eff}}$ . The filled circles represent stars for which data at band 4 (0.6–0.8 MHz) are available. The two unfilled diamonds are for  $\rho$  Oph A (data correspond to 2.1 GHz) and HD 142301 (data correspond to 1.5 GHz). The solid line corresponds to the relation  $S_{\text{peak}} d^2 \propto X^{0.8 \pm 0.1}$ , where  $X = B_0^{\text{max}} / (T_{\text{eff}} - 16.5)^2$ . The surrounding shaded regions around the solid line show the  $3\sigma$  uncertainty. The outlier around  $X = 0.14$  corresponds to HD 147933. See Section 5.2.1 for details.

ingredient for triggering ECME. However, other than determining the frequency of emission, the absolute value of the dipole strength does not play a role in the ECME growth rate (e.g., Lee et al. 2013). Keeping the observation frequency constant, when we compare ECME luminosity in stars with different dipole strengths, we effectively compare luminosity for ECME produced at different heights from the stellar surface. Thus the correlation with magnetic field strength directly translates to the statement that the peak ECME luminosity increases as we go farther from the stellar surface. If this statement holds, it should also be reflected in the ECME spectrum of individual stars (in the form of a negative spectral index). However for the few MRPs for which ECME spectra have been reported, such behavior has only been observed close to the upper cutoff frequencies (much higher than the frequency range of band 4, Das et al. 2020a; Das & Chandra 2021). This rules out the interpretation that the correlation with surface magnetic field strength signifies a dependence on the height of the emission sites from the stellar surface.

There is however an alternate way to view this correlation, which involves the process that energizes the electrons. Leto et al. (2021) demonstrated that gyrosynchrotron luminosity scales strongly with the unsigned magnetic flux ( $B_d R_*^2$ ) and rotation. The relation with the latter led them to speculate that centrifugal breakout (CBO) events, previously shown by Shultz et al. (2020) and Owocki et al. (2020) to regulate H $\alpha$  emission, may be the source of electron acceleration, a scenario that has been worked out in detail by M. E. Shultz et al. (2021, in preparation) In that case, the stronger the surface magnetic field, the larger the Alfvén radius  $R_A$ , and the higher the rotational energy of the co-rotating plasma near  $R_A$ . Thus, the energy involved in CBO events in a star with a stronger surface magnetic field is very likely higher than that in a star with a weaker magnetic field (M. E. Shultz et al. 2021, in preparation). With a larger energy reservoir, more electrons can be energized, which might be the root of the origin of the observed empirical relation between peak ECME luminosity and the surface magnetic field strength.

Unlike that for  $B_0^{\max}$ , the relation between the ECME luminosity and temperature is nonmonotonic. One probable scenario is that for very low  $T_{\text{eff}}$ , the stellar wind is weak so that there are not enough particles to emit ECME. For a very high  $T_{\text{eff}}$ , the wind will be stronger, the magnetosphere will be denser, and the associated absorption of the radio emission is likely to increase. Besides, with increasing plasma density, it becomes increasingly difficult to maintain the necessary condition of  $\nu_p < \nu_B$ , where  $\nu_p$  and  $\nu_B$  are respectively the plasma and electron gyrofrequencies.

Our finding of the dependence of the peak ECME luminosity on temperature is in stark contrast to the scaling relation obtained for gyrosynchrotron emission by Leto et al. (2021), where the only physical parameters involved are the magnetic flux and rotation period. This is consistent with the idea proposed by Leto et al. (2021) that the incoherent and coherent parts of the radio emission are produced by different populations of electrons and at different sites of the stellar magnetosphere. A rigorous conclusion, however, can only be drawn following a similar analysis with a larger sample of MRPs.

In the past, there has been only one magnetic hot star where ECME was reported to be absent: HD 37479 ( $\sigma$  Ori E;

Leto et al. 2012). The lowest frequency observed by Leto et al. (2012) was 1.4 GHz. The absence of ECME was attributed to the presence of higher-order moments in the stellar magnetic field. It is however yet to be examined whether the star produces ECME at sub-GHz frequencies. For this star, using the available measurements for the stellar  $B_0^{\max}$  and  $T_{\text{eff}}$  (Oksala et al. 2012; Shultz et al. 2019b, 2019a; Oksala et al. 2015), we obtain  $X=0.24$ . From Figure 11 and using the known distance to the star (Gaia Collaboration et al. 2018), we find that the peak ECME flux density (if it indeed produces ECME) will be only a few mJy or less. This is consistent with the fact that no ECME pulse has been observed from the star at frequencies  $\geq 1.4$  GHz since the basal flux density of the star at 1.4 GHz itself varies between 2 and 3 mJy (Leto et al. 2012). Nevertheless, it will be highly important to observe the star at lower radio frequencies, especially to check the validity of our empirical relation.

Another star that has been observed for nearly a full rotation cycle at higher radio frequencies, but is yet to be observed in detail at lower frequencies, is HD 182180. Radio observations covering nearly the full stellar rotation cycle were reported by Leto et al. (2017) at 6–44 GHz. The lowest frequency of their observation (6 GHz) is higher than the typical cutoff frequencies observed for MRPs (e.g., Das et al. 2020a). Thus it is not a surprise that ECME was not observed from this star at those frequencies. For this star also, we attempt to examine whether it is likely to produce detectable ECME at lower radio frequencies. We use the measurements reported in Oksala et al. (2010) and Rivinius et al. (2010, 2013) to find  $X=0.9$ . The predicted peak ECME flux density (in excess of the basal gyrosynchrotron flux density) of the star comes out to be  $\lesssim 5$  mJy (after we use the distance from Gaia Collaboration et al. 2018). Since, at sub-Hz frequencies, one does not see detectable modulation of gyrosynchrotron emission, it is a promising candidate to observe at low radio frequencies.

Finally, we consider the star HD 61556 (HR 2949) that has been recently detected in the circular polarization survey carried out with the Australian Square Kilometre Array Pathfinder (ASKAP) telescope at 887.5 MHz (Pritchard et al. 2021). The reported circular polarization is  $76 \pm 16\%$  (Pritchard et al. 2021), which makes it a highly likely MRP candidate. For this star, we find  $X=0.7$  (values of the stellar parameters are taken from Shultz et al. 2015, 2019b, 2019a). This implies that the peak ECME flux density from this star would be  $\sim 10$  mJy (after we use the distance from Gaia Collaboration et al. 2018), which independently predicts that this star is a MRP.

A limitation of this analysis is that the peak flux densities of ECME pulses are known to be variable (e.g., Trigilio et al. 2011; Das & Chandra 2021). This makes the quantitative prediction of the peak ECME flux density for a given star from our empirical relation somewhat unreliable. However the usefulness of a relation like the one depicted in Figure 11 lies in its ability to predict whether a magnetic hot star is likely to produce coherent radio emission or not.

To summarize, our analysis, based on the data for 14 of the 15 MRPs, suggests that the primary physical quantities that determine whether ECME from a star will be detectable or not are the maximum surface magnetic field strength and the surface temperature. While the efficiency of the phenomenon appears to increase monotonically with increasing magnetic field strength, it reaches a maximum around a surface temperature of 16–17 kK. To examine the robustness of these

inferences (and also to be able to predict whether a hot magnetic star will produce detectable ECME or not), it will be important to continue searching for more of these objects.

### 5.2.2. Influence of the Obliquity on the ECME Pulse Profiles

One interesting suggestion that has come out of this work is the influence of the stellar obliquity  $\beta$ , i.e., the angle between the magnetic dipole and rotation axes, on the ECME pulse profile. Five stars in our sample have  $\beta$  close to  $90^\circ$ : HD 12447, HD 19832, HD 79158, HD 145501C, and HD 176582 (Table 1). The latter has however only a partially covered ECME pulse profile (Figure 8) and hence will not be included in this discussion. Previously, only one MRP, HD 142990, which has an obliquity close to  $90^\circ$  (Shultz et al. 2019a), was known (Lenc et al. 2018; Das et al. 2019a). The four stars HD 142990, HD 12447, HD 19832, and HD 145501C exhibit highly peculiar pulse profiles, characterized by clearly separated subpulses (at the same polarization) instead of a single pulse (e.g., compare Figures 2 and 4). HD 79158 is apparently an exception from this point as we did not observe such a feature in its pulses (Figure 5). However, a confirmed inference can only be drawn after we observe the star over the broader rotational phase window. The peculiar pulse profiles in stars with  $\beta \approx 90^\circ$  is consistent with the simulation results of Das et al. (2020b), where they showed that a large obliquity might lead to highly nonintuitive ECME pulse characteristics, purely due to propagation effects in the magnetosphere. Thus, in the future, it will be important to conduct a study including MRPs with such large obliquities (e.g.,  $>85^\circ$ ) to understand how this aspect of the stellar magnetosphere influences the ECME characteristics.

Physically one can understand this effect by considering the fact that the plasma distribution in the stellar magnetosphere is a strong function of the obliquity (e.g., Townsend & Owocki 2005). For the case where the rotation and dipole axes are aligned, the distribution (theoretically) is symmetric about the magnetic/rotation axes. It is characterized by the presence of a dense disk in the magnetic/rotational equatorial plane and, away from that, the density falls sharply (Townsend & Owocki 2005). However, when the two axes are not aligned, the distribution loses the symmetry. The disk-like overdensity no longer remains at the magnetic equator (e.g., see Figure 9 of Das et al. 2020b). The case when the obliquity is  $90^\circ$  is an extreme situation and it is still not clear how the plasma will organize itself in such a case. But according to the semi-analytical “Rigidly Rotating Magnetosphere” (RRM) model of Townsend & Owocki (2005), in such a case, the disk gets warped with increasing  $\beta$  and becomes two cones when  $\beta = 90^\circ$  (see Figure 3 of Townsend & Owocki 2005). The double ECME pulses observed from stars with obliquities  $\approx 90^\circ$  might be a signature of such a density distribution in the stellar magnetosphere.

It is however to be noted that whether or not the ray path corresponding to the observed emission will pass through regions with high density gradients is likely to be dependent on other stellar parameters as well, like the inclination angle  $i$  and the rotation period  $P_{\text{rot}}$ . Together with the stellar mass and radius, the latter defines the Kepler radius  $R_K$ , which is the distance at which the centrifugal force due to co-rotation balances gravity. According to the RRM model of Townsend & Owocki (2005), plasma cannot accumulate at distances smaller than  $\approx 0.87R_K$ . Thus for two stars with similar physical

parameters except for  $P_{\text{rot}}$ , the slower rotator will have a larger  $R_K$ , and hence a smaller extent of the plasma disk. For a more rapid rotator, the probability that the observed radiation has to pass through the overdense region will be higher. To summarize, a large misalignment between rotation and dipole axes will not necessarily lead to a peculiar pulse profile; however a peculiar pulse profile is very likely an indicator of large obliquity. Once again, a larger sample of MRPs will be very helpful to disentangle the effects of inclination angle, obliquity, and rotation period.

### 5.3. Lack of High Circular Polarization

Our results show that 100% circular polarization is not a necessary criterion to identify MRP candidates. In the ideal case of a star with an axi-symmetric magnetic field, the net circular polarization in the observed pulses will be zero when the radiation coming from the opposite magnetic hemisphere suffers no deviation at all on its way toward the observer (Leto et al. 2016). Most recently, Das et al. (2020b) showed via simulation that the radiation may experience significant deviation in the stellar magnetosphere, and yet the net circular polarization can be much smaller (see the bottom panel of their Figure 10). This is consistent with the fact that for the star HD 12447, the observed circular polarization is quite small, and also the pulse profiles are peculiar; the latter being indicative of the experience of significant propagation effects in the stellar magnetosphere (Das et al. 2020b).

### 5.4. Effect of Complex Surface Magnetic Field

Among the eight MRPs that we report in this paper, only two (HD 12447 and HD 19832) exhibit  $\langle B_z \rangle$  modulation that can be reasonably well fitted by assuming a dipolar surface magnetic field. But in these two cases, the error bars in the  $\langle B_z \rangle$  values are much larger than those for the other stars so that the “good fit” obtained using a sinusoidal function might be a “limitation” of that. Among the already known MRPs, CU Vir, HD 133880, HD 142990, and HD 35298 are known to possess magnetic fields more complex than that of an axi-symmetric dipole (Kochukhov et al. 2014, 2017; Shultz et al. 2018). Thus we do not have any evidence of higher-order magnetic moments suppressing ECME. Furthermore, offsets of the rotational phases of arrival of ECME pulses from their predicted values (close to the magnetic nulls) have been attributed to complex surface magnetic fields (e.g., Leto et al. 2019; Das et al. 2019a). We, however, observed ECME pulses right at the magnetic nulls for several of the eight stars with complex surface magnetic fields (e.g., HD 45583), but away from the magnetic null for one (HD 12447) of the two stars exhibiting apparently sinusoidal  $\langle B_z \rangle$  variation. Thus, it appears that the offset in the rotational phases of arrival of ECME pulses is not exclusively dependent on the magnetic field topology, but on other stellar physical parameters. For example, in case of HD 12447, we propose that the star’s large obliquity is behind its peculiar pulse characteristics. Sometimes, the offsets could be artificial, e.g., due to the use of an insufficiently precise ephemeris.

One caveat here is that with increasing distance, the higher-order magnetic moments decay faster than the dipolar moment, so that below a certain radio frequency, the magnetic field will effectively be dipolar. Since we are comparing stars with different  $B_0^{\text{max}}$ , the same observation frequency corresponds to different heights from the stellar surface. For example,

assuming a dipolar geometry and emission at the fundamental harmonic, an observation frequency of 0.7 GHz corresponds to a height of  $2.3 R_*$  for HD 45583 ( $B_d = 9.1$  kG, Table 1) and  $0.9 R_*$  for HD 170000 ( $B_d = 1.8$  kG, Table 1) from the stellar surface. However even if we compare stars with similar  $B_0^{\max}$  (e.g., HD 12447 and HD 170000), the discrepancy described above remains.

### 5.5. Suitable Observation Strategy

One important issue raised in this paper is the lack of a strategy to search for this phenomenon that will be suitable for any magnetic hot star. Since it is now well accepted that the radio pulses due to ECME can be visible at rotational phases that are offset from the magnetic null phases, one cannot rule out the existence of the phenomenon by merely observing a star over a specific rotational phase window. Besides, for the MRP CU Vir, the ECME pulses at 2.3 GHz have been found to be intermittent (Ravi et al. 2010). That is why the ideal way to find out if a star produces ECME or not is to observe the star over as large a rotational phase window (around the magnetic nulls) as possible (preferably for one full rotation cycle). Even then, it remains difficult to completely rule out the phenomenon due to our lack of understanding regarding the ECME cutoff frequencies. Based on the currently available data, it appears that ECME is favored at frequencies  $\lesssim 5$  GHz. Unfortunately a similar estimate for the lower limit to the suitable observing frequency is not available, as barring HD 133880, the lower cutoff frequency of ECME from other MRPs has not been observed. In the case of HD 133880, Das et al. (2020a) reported that one of the ECME pulses has a tentative lower cutoff frequency at around 0.4 GHz, though for the other pulses, the lower cutoff frequency is clearly below 0.4 GHz. The lowest frequency of observation of ECME from MRPs is 0.2 GHz (HD 142990, Lenc et al. 2018). To the best of our knowledge, no detailed study (e.g., obtaining the lightcurves) has been performed for MRPs below 0.4 GHz. To understand the low frequency characteristics of ECME, it will be important to study the known MRPs below their current lowest frequencies of observation.

Though we have some handle on choosing the observing frequency, observing each star for one complete rotation cycle to overcome the issue of the offset in the rotational phases of arrival of the pulses is practically impossible. This is especially the case for a survey of slowly rotating stars (which can have periods up to several decades). In such a case, one way to proceed will be to choose any one of the stellar magnetic nulls and observe for as much time as possible around it (this strategy was adopted for HD 19832, HD 145501C, and HD 45583). The limitation of this strategy is that it might give a false nondetection for stars that, like CU Vir, exhibit intermittent ECME pulses. An alternate way for discovering more MRPs is to use sky surveys. The MRP HD 142990 was first identified as a candidate when it was detected in an all-sky circular polarization survey carried out with the Murchison Widefield Array (Lenc et al. 2018). Recently, Pritchard et al. (2021) reported the detection of three magnetic chemically peculiar stars (that were not detected in the radio previously) in the circular polarization survey conducted with the ASKAP telescope. All three stars are potential MRPs and require targeted observation. This strategy has the disadvantage of excluding MRPs that do not give rise to high circular polarization. More importantly, such surveys are not scheduled

to target a particular rotational phase range of individual stars (e.g., around the magnetic null phases), which is likely to affect the detection rate significantly. Nevertheless, for increasing the sample size of MRPs, circular polarization sky surveys, followed by targeted observation, seems to be a useful supplement to targeted observations of well-characterized magnetic stars.

## 6. Conclusion

The primary results and the conclusions drawn from this work are listed below:

1. More than doubling the sample of MRPs: we report eight new MRPs, HD 12447, HD 37017, HD 19832 HD 45583, HD 79158, HD 145501C, HD 170000, and HD 176582. This makes the total number of known MRPs 15. Out of these eight stars reported here, 10 are discovered and one is confirmed using the GMRT.
2. ECME is not a rare phenomenon: we find that at least 32% of magnetic hot stars with physical properties within the ranges spanned by the sample of MRPs, and with visible magnetic nulls, exhibit ECME.
3. Onset of ECME: for the first time, we perform a comparative analysis using 14 of the 15 MRPs and present an empirical relation to predict whether a hot magnetic will produce detectable ECME. Our preliminary analysis suggests that the efficiency of the phenomenon is primarily controlled by the stellar magnetic field strength and the surface temperature.
4.  $T_{\text{eff}}$  corresponding to maximum ECME luminosity: our analysis suggests that the peak ECME luminosity reaches its maximum in stars with  $T_{\text{eff}} \approx 16\text{--}17$  kK.
5. Influence of magnetospheric plasma distribution on the ECME pulse profile: we find that all three MRPs (HD 142990, HD 19832, and HD 145501C), whose pulses are fully covered by observation and with obliquity  $\approx 90^\circ$ , exhibit “double-pulse” profiles (e.g., see Figures 2 and 6). In addition, no other MRP has been found to exhibit this characteristic. Since obliquity plays an important role in shaping the magnetospheric plasma distribution, this observation demonstrates the importance of propagation effects in the stellar magnetosphere on the ECME pulse profile.
6. Effect of complex stellar magnetic field: based on the current data, we do not find any evidence of any definitive role of higher-order magnetic moments in suppressing the onset of ECME. Our results also disfavor the idea of complex stellar magnetic fields causing offsets in the rotational phases of arrival of ECME.

Lastly, we would like to reiterate the need to increase the sample size of MRPs. Our work clearly suggests that it is not a rare phenomenon, and the primary difficulty lies in coming up with a suitable strategy to observe these stars.

We acknowledge support of the Department of Atomic Energy, Government of India, under project no. 12-R&D-TFR-5.02-0700. B.D. thanks David Bohlender for suggesting the star HD 79158 to observe in radio bands. P.C. acknowledges support from the Department of Science and Technology via SwarnaJayanti Fellowship awards (DST/SJF/PSA-01/2014-15). M.E.S. acknowledges support from the Annie Jump Cannon Fellowship, supported by the University of Delaware

**Table 3**  
Observation Log of HD 37017

HJD−2,457,300	$\phi_{\text{rot}}$	$n$	$\langle B_z \rangle$ (G)	DF (V)	$\langle N_z \rangle$ (G)	DF (N)
25.04535	0.19	6	$-869 \pm 132$	DD	$130 \pm 140$	ND
29.09279	0.68	6	$-69 \pm 126$	DD	$15 \pm 130$	ND
30.09825	0.80	6	$-720 \pm 136$	DD	$120 \pm 140$	ND
31.13575	0.95	12	$-1186 \pm 107$	DD	$70 \pm 110$	ND

**Note.** The term  $\phi_{\text{rot}}$  represents the rotational phase calculated using the ephemeris given in Table 1, and  $n$  gives the number of spectropolarimetric sequences comprising each measurement. DF gives the Detection Flag, either a Non-Detection (ND) or Definite Detection (DD).

and endowed by the Mount Cuba Astronomical Observatory. G.A.W. acknowledges Discovery Grant support from the Natural Sciences and Engineering Research Council (NSERC) of Canada. We thank the staff of the GMRT that made our observations possible. The GMRT is run by the National Centre for Radio Astrophysics of the Tata Institute of Fundamental Research. The National Radio Astronomy Observatory is a facility of the National Science Foundation operated under cooperative agreement by Associated Universities, Inc. This research has made use of NASA's Astrophysics Data System.

### Appendix Spectropolarimetric Measurements of HD 37017

Twelve magnetic measurements obtained with the ESPaDOnS spectropolarimeter were previously published by Shultz et al. (2018). ESPaDOnS (Échelle Spectropolarimetric Device for the Observation of Stars) is a high-resolution ( $\lambda/\Delta\lambda \sim 65,000$ ) échelle spectropolarimeter mounted at the Canada–France–Hawaii Telescope (CFHT). The instrument covers the wavelength range from 370 nm to 1050 nm over 40 overlapping spectral orders. Each spectropolarimetric sequence consists of four differently polarized subexposures, which can be combined to yield a circular polarization (Stokes  $V$ ) spectrum, or a null polarization ( $N$ ) spectrum in which intrinsic polarization from the source is canceled out, thereby giving a measurement of the noise and a check on normal instrument observation. The characteristics of ESPaDOnS and the Libre-ESpRIT reduction pipeline were described in detail by Wade et al. (2016).

Between 2015 October 29 and 2015 November 3 a further 42 ESPaDOnS observations of HD 37017 were acquired by the BinaMIcS (Binarity and Magnetic Interactions in various classes of Stars; Alecian et al. 2015) Large Program. Each observation consisted of  $4 \times 50$  s subexposures. The observations were taken on four nights, with between 30 and 68 minutes between the start and end of each set of observations. As this corresponds to between 0.02 and 0.05 of a rotational cycle, observations acquired on a single night were co-added in order to increase the signal-to-noise ratio (S/N). The observation log is given in Table 3.

To increase the S/N sufficiently to detect and measure the magnetic field, Least-Squares Deconvolution (LSD; Donati et al. 1997) mean line profiles were extracted, using the iLSD package developed by Kochukhov et al. (2010). The line list was the same as the one used by Shultz et al. (2018), originally obtained from Vienna Atomic Lines Database (VALD3; Piskunov et al. 1995; Ryabchikova et al. 1997; Kupka et al. 1999, 2000; Ryabchikova et al. 2015), and then cleaned to remove contaminating Balmer, He, and telluric features. Due to the broad stellar lines, LSD profiles were extracted using

$7.2 \text{ km s}^{-1}$  velocity pixels, i.e., four times the usual pixel size; this provided a per-pixel S/N boost of a factor of 2, at the expense of velocity resolution. Evaluation of False Alarm Probabilities using the method and criteria described by Donati et al. (1992, 1997) found 4/4 Stokes  $V$  profiles to be definite detections (DD), and all 4  $N$  profiles to be NDs as expected (Table 3).

Since HD 37017 is a double-lined spectroscopic binary with an 18 day orbit (Bolton et al. 1998), it was also necessary to remove the contribution of the nonmagnetic companion from the Stokes  $I$  profile. Radial velocities of the components were measured using the parameterized line profile fitting routine described by Grunhut et al. (2017), and the line profiles were then disentangled (using the full data set, i.e., including the ESPaDOnS measurements analyzed earlier) using the same iterative procedure as adopted by Shultz et al. (2018). The longitudinal magnetic field averaged over the stellar disk  $\langle B_z \rangle$  (Mathys 1989) was measured from the disentangled line profiles in order to quantify the line-of-sight magnetic field strength. The same measurement was performed using  $N$ , yielding  $\langle N_z \rangle$ .  $\langle B_z \rangle$  and  $\langle N_z \rangle$  measurements are given in Table 3.

### ORCID iDs

Barnali Das  <https://orcid.org/0000-0001-8704-1822>  
Poonam Chandra  <https://orcid.org/0000-0002-0844-6563>  
Matt E. Shultz  <https://orcid.org/0000-0003-1387-5044>  
Gregg A. Wade  <https://orcid.org/0000-0002-1854-0131>  
James Sikora  <https://orcid.org/0000-0002-3522-5846>  
Oleg Kochukhov  <https://orcid.org/0000-0003-3061-4591>  
Coralie Neiner  <https://orcid.org/0000-0003-1978-9809>  
Mary E. Oksala  <https://orcid.org/0000-0003-2580-1464>  
Evelyne Alecian  <https://orcid.org/0000-0001-5260-7179>

### References

- Alecian, E., Wade, G. A., Catala, C., et al. 2013, *MNRAS*, **429**, 1001  
Alecian, E., Neiner, C., Wade, G. A., et al. 2015, in *New windows on massive stars: asteroseismology, interferometry, and spectropolarimetry*, Proc. of the IAU Symp. 307, ed. G. Meynet et al. (Cambridge: Cambridge Univ. Press), 330  
Aurière, M., Wade, G. A., Silvester, J., et al. 2007, *A&A*, **475**, 1053  
Bagnulo, S., Fossati, L., Landstreet, J. D., & Izzo, C. 2015, *A&A*, **583**, A115  
Bernhard, K., Hümmerich, S., & Paunzen, E. 2020, *MNRAS*, **493**, 3293  
Bohlender, D. A., Brown, D. N., Landstreet, J. D., & Thompson, I. B. 1987, *ApJ*, **323**, 325  
Bohlender, D. A., Landstreet, J. D., & Thompson, I. B. 1993, *A&A*, **269**, 355  
Bohlender, D. A., & Monin, D. 2011, *AJ*, **141**, 169  
Bolton, C. T., Harmanec, P., Lyons, R. W., Odell, A. P., & Pyper, D. M. 1998, *A&A*, **337**, 183  
Borra, E. F., & Landstreet, J. D. 1979, *ApJ*, **228**, 809  
Borra, E. F., & Landstreet, J. D. 1980, *ApJS*, **42**, 421  
Borra, E. F., Landstreet, J. D., & Thompson, I. 1983, *ApJS*, **53**, 151  
Bychkov, V. D., Bychkova, L. V., & Madej, J. 2021, *A&A*, **652**, A31

- Capitaino, L., Lalletment, R., Vergely, J. L., Elyajouri, M., & Monreal-Ibero, A. 2017, *A&A*, **606**, A65
- Chandra, P., Wade, G. A., Sundqvist, J. O., et al. 2015, *MNRAS*, **452**, 1245
- Chojnowski, S. D., Hubrig, S., Hasselquist, S., et al. 2019, *ApJL*, **873**, L5
- Das, B., & Chandra, P. 2021, *ApJ*, **921**, 9
- Das, B., Chandra, P., Shultz, M. E., & Wade, G. A. 2019a, *ApJ*, **877**, 123
- Das, B., Chandra, P., Shultz, M. E., & Wade, G. A. 2019b, *MNRAS*, **489**, L102
- Das, B., Chandra, P., & Wade, G. A. 2018, *MNRAS*, **474**, L61
- Das, B., Chandra, P., & Wade, G. A. 2020a, *MNRAS*, **499**, 702
- Das, B., Mondal, S., & Chandra, P. 2020b, *ApJ*, **900**, 156
- Dodge, Y. 2008, *Spearman Rank Correlation Coefficient* (New York, NY: Springer), 502
- Donati, J.-F., Semel, M., Carter, B. D., Rees, D. E., & Collier Cameron, A. 1997, *MNRAS*, **291**, 658
- Donati, J.-F., Semel, M., & Rees, D. E. 1992, *A&A*, **265**, 669
- Drake, S. A., Abbott, D. C., Bastian, T. S., et al. 1987, *ApJ*, **322**, 902
- Gaia Collaboration, Brown, A. G. A., Vallenari, A., et al. 2018, *A&A*, **616**, A1
- Gaia Collaboration, Smart, R. L., Sarro, L. M., et al. 2021, *A&A*, **649**, A6
- Grunhut, J. H., Wade, G. A., Neiner, C., et al. 2017, *MNRAS*, **465**, 2432
- Hallinan, G., Antonova, A., Doyle, J. G., et al. 2006, *ApJ*, **653**, 690
- Kochukhov, O., & Bagnulo, S. 2006, *A&A*, **450**, 763
- Kochukhov, O., Lüftinger, T., Neiner, C., Alecian, E. & MiMeS Collaboration 2014, *A&A*, **565**, A83
- Kochukhov, O., Makaganiuk, V., & Piskunov, N. 2010, *A&A*, **524**, A5
- Kochukhov, O., Shultz, M., & Neiner, C. 2019, *A&A*, **621**, A47
- Kochukhov, O., Silvester, J., Bailey, J. D., Land Street, J. D., & Wade, G. A. 2017, *A&A*, **605**, A13
- Kounkel, M., Hartmann, L., Loinard, L., et al. 2017, *ApJ*, **834**, 142
- Kudryavtsev, D. O., Romanyuk, I. I., Elkin, V. G., & Paunzen, E. 2006, *MNRAS*, **372**, 1804
- Kupka, F. G., Piskunov, N., Ryabchikova, T. A., Stempels, H. C., & Weiss, W. W. 1999, *A&AS*, **138**, 119
- Kupka, F. G., Ryabchikova, T. A., Piskunov, N. E., Stempels, H. C., & Weiss, W. W. 2000, *BaltA*, **9**, 590
- Lalletment, R., Capitaino, L., Ruiz-Dern, L., et al. 2018, *A&A*, **616**, A132
- Lalletment, R., Vergely, J. L., Valette, B., et al. 2014, *A&A*, **561**, A91
- Landstreet, J. D., Bagnulo, S., Andretta, V., et al. 2007, *A&A*, **470**, 685
- Landstreet, J. D., & Borra, E. F. 1977, *ApJL*, **212**, L43
- Landstreet, J. D., & Mathys, G. 2000, *A&A*, **359**, 213
- Landstreet, J. D., Silaj, J., Andretta, V., et al. 2008, *A&A*, **481**, 465
- Lee, S.-Y., Yi, S., Lim, D., et al. 2013, *JGRA*, **118**, 7036
- Lenc, E., Murphy, T., Lynch, C. R., Kaplan, D. L., & Zhang, S. N. 2018, *MNRAS*, **478**, 2835
- Leone, F., Triglio, C., Neri, R., & Umana, G. 2004, *A&A*, **423**, 1095
- Leone, F., & Umana, G. 1993, *A&A*, **268**, 667
- Leto, P., Triglio, C., Buemi, C. S., et al. 2020b, *MNRAS*, **499**, L72
- Leto, P., Triglio, C., Buemi, C. S., et al. 2016, *MNRAS*, **459**, 1159
- Leto, P., Triglio, C., Buemi, C. S., Leone, F., & Umana, G. 2012, *MNRAS*, **423**, 1766
- Leto, P., Triglio, C., Buemi, C. S., Umana, G., & Leone, F. 2006, *A&A*, **458**, 831
- Leto, P., Triglio, C., Krtićka, J., et al. 2021, *MNRAS*, **507**, 1979
- Leto, P., Triglio, C., Leone, F., et al. 2020a, *MNRAS*, **493**, 4657
- Leto, P., Triglio, C., Oskinova, L., et al. 2017, *MNRAS*, **467**, 2820
- Leto, P., Triglio, C., Oskinova, L. M., et al. 2018, *MNRAS*, **476**, 562
- Leto, P., Triglio, C., Oskinova, L. M., et al. 2019, *MNRAS*, **482**, L4
- Lim, J., Drake, S. A., & Linsky, J. L. 1996, in *ASP Conf. Ser.*, **93**, Rotational Modulation of Radio Emission from the Magnetic BP Star HR 5624, ed. A. R. Taylor & J. M. Paredes (San Francisco, CA: ASP), 324
- Linsky, J. L., Drake, S. A., & Bastian, T. S. 1992, *ApJ*, **393**, 341
- Lynch, C. R., Lenc, E., Kaplan, D. L., Murphy, T., & Anderson, G. E. 2017, *ApJL*, **836**, L30
- Mathys, G. 1989, *FCPh*, **13**, 143
- Mathys, G. 2017, *A&A*, **601**, A14
- McMullin, J. P., Waters, B., Schiebel, D., Young, W., & Golap, K. 2007, in *ASP Conf. Series*, Vol. 376, *Astronomical Data Analysis Software and Systems XVI*, ed. R. A. Shaw, F. Hill, & D. J. Bell (San Francisco, CA: ASP), 127
- Melrose, D. B., & Dulk, G. A. 1982, *ApJ*, **259**, 844
- Moiseeva, A. V., Romanyuk, I. I., Semenko, E. A., Kudryavtsev, D. O., & Yakunin, I. A. 2019, *AstBu*, **74**, 62
- Munoz, M. S., Wade, G. A., Nazé, Y., et al. 2020, *MNRAS*, **492**, 1199
- Musielok, B. 1986, *AcA*, **36**, 131
- Napiwotzki, R., Schoenberner, D., & Wenske, V. 1993, *A&A*, **268**, 653
- Netopil, M., Paunzen, E., Hümmerich, S., & Bernhard, K. 2017, *MNRAS*, **468**, 2745
- Netopil, M., Paunzen, E., Maitzen, H. M., North, P., & Hubrig, S. 2008, *A&A*, **491**, 545
- Oksala, M. E., Kochukhov, O., Krtićka, J., et al. 2015, *MNRAS*, **451**, 2015
- Oksala, M. E., Silvester, J., Kochukhov, O., et al. 2018, *MNRAS*, **473**, 3367
- Oksala, M. E., Wade, G. A., Marcolino, W. L. F., et al. 2010, *MNRAS*, **405**, L51
- Oksala, M. E., Wade, G. A., Townsend, R. H. D., et al. 2012, *MNRAS*, **419**, 959
- Owocik, S. P., Shultz, M. E., ud-Doula, A., et al. 2020, *MNRAS*, **499**, 5366
- Paunzen, E. 2015, *A&A*, **580**, A23
- Petit, V., Owocik, S. P., Wade, G. A., et al. 2013, *MNRAS*, **429**, 398
- Piskunov, N. E., Kupka, F., Ryabchikova, T. A., Weiss, W. W., & Jeffery, C. S. 1995, *A&AS*, **112**, 525
- Pritchard, J., Murphy, T., Zic, A., et al. 2021, *MNRAS*, **502**, 5438
- Ravi, V., Hobbs, G., Wickramasinghe, D., et al. 2010, *MNRAS*, **408**, L99
- Rivinius, T., Szeifert, T., Barrera, L., et al. 2010, *MNRAS*, **405**, L46
- Rivinius, T., Townsend, R. H. D., Kochukhov, O., et al. 2013, *MNRAS*, **429**, 177
- Romanyuk, I. I. 2019, *AstBu*, **74**, 437
- Romanyuk, I. I., Moiseeva, A. V., Semenko, E. A., Kudryavtsev, D. O., & Yakunin, I. A. 2020, *AstBu*, **75**, 294
- Romanyuk, I. I., Semenko, E. A., & Kudryavtsev, D. O. 2014, *AstBu*, **69**, 427
- Romanyuk, I. I., Semenko, E. A., & Kudryavtsev, D. O. 2015, *AstBu*, **70**, 444
- Romanyuk, I. I., Semenko, E. A., Kudryavtsev, D. O., Moiseeva, A. V., & Yakunin, I. A. 2017a, *AstBu*, **72**, 391
- Romanyuk, I. I., Semenko, E. A., Kudryavtsev, D. O., & Moiseeva, A. V. 2016a, *AstBu*, **71**, 302
- Romanyuk, I. I., Semenko, E. A., Moiseeva, A. V., Kudryavtsev, D. O., & Yakunin, I. A. 2018, *AstBu*, **73**, 178
- Romanyuk, I. I., Semenko, E. A., Moiseeva, A. V., Yakunin, I. A., & Kudryavtsev, D. O. 2019, *AstBu*, **74**, 55
- Romanyuk, I. I., Semenko, E. A., Moiseeva, A. V., Yakunin, I. A., & Kudryavtsev, D. O. 2021, *AstBu*, **76**, 39
- Romanyuk, I. I., Semenko, E. A., Yakunin, I. A., Kudryavtsev, D. O., & Moiseeva, A. V. 2016b, *AstBu*, **71**, 436
- Romanyuk, I. I., Semenko, E. A., Yakunin, I. A., Kudryavtsev, D. O., & Moiseeva, A. V. 2017b, *AstBu*, **72**, 165
- Ryabchikova, T., Piskunov, N., Kurucz, R. L., et al. 2015, *PhyS*, **90**, 054005
- Ryabchikova, T. A., Piskunov, N. E., Kupka, F., & Weiss, W. W. 1997, *BaltA*, **6**, 244
- Semenko, E. A., Kudryavtsev, D. O., Ryabchikova, T. A., & Romanyuk, I. I. 2008, *AstBu*, **63**, 128
- Shultz, M., Rivinius, T., Folsom, C. P., et al. 2015, *MNRAS*, **449**, 3945
- Shultz, M. E., Wade, G. A., Rivinius, T., et al. 2018, *MNRAS*, **475**, 5144
- Shultz, M. E., Wade, G. A., Rivinius, T., et al. 2019a, *MNRAS*, **490**, 274
- Shultz, M. E., Wade, G. A., Rivinius, T., et al. 2019b, *MNRAS*, **485**, 1508
- Shultz, M. E., Owocik, S., Rivinius, T., et al. 2020, *MNRAS*, **499**, 5379
- Sikora, J., Wade, G. A., Power, J., & Neiner, C. 2019a, *MNRAS*, **483**, 3127
- Sikora, J., Wade, G. A., Power, J., & Neiner, C. 2019b, *MNRAS*, **483**, 2300
- Townsend, R. H. D., & Owocik, S. P. 2005, *MNRAS*, **357**, 251
- Triglio, C., Leto, P., Leone, F., Umana, G., & Buemi, C. 2000, *A&A*, **362**, 281
- Triglio, C., Leto, P., Umana, G., Buemi, C. S., & Leone, F. 2011, *ApJL*, **739**, L10
- Triglio, C., Leto, P., Umana, G., Leone, F., & Buemi, C. S. 2004, *A&A*, **418**, 593
- van Leeuwen, F. 2007, *A&A*, **474**, 653
- Wade, G. A., Smith, M. A., Bohlender, D. A., et al. 2006, *A&A*, **458**, 569
- Wade, G. A., Neiner, C., Alecian, E., et al. 2016, *MNRAS*, **456**, 2
- Worthey, G., & Lee, H.-c. 2011, *ApJS*, **193**, 1